ARIEL Electron to Gamma Converter Design

by

Marla Stephanie Cervantes Smith
B.Sc., Universidad Autonoma de Yucatan, 2013

A Thesis Submitted in Partial Fulfillment of the
Requirements for the Degree of

MASTER OF SCIENCE

in the Department of Physics and Astronomy

University of Victoria

ARIEL Electron to Gamma Converter Design

by

Marla Stephanie Cervantes Smith
B.Sc., Universidad Autonoma de Yucatan, 2013

Supervisory Committee

Dr. Dean Karlen, Co-Supervisor
(Department of Physics and Astronomy)

Dr. Alexander Gottberg, Co-Supervisor
(Department of Physics and Astronomy)

Dr. Robert Kowalewski, Departmental Member
(Department of Physics and Astronomy)

Supervisory Committee

Dr. Dean Karlen, Co-Supervisor
(Department of Physics and Astronomy)

Dr. Alexander Gottberg, Co-Supervisor
(Department of Physics and Astronomy)

Dr. Robert Kowalewski, Departmental Member
(Department of Physics and Astronomy)

ABSTRACT

The e-linac beam that will serve the ARIEL Electron Target East (AETE) has an energy range from 30 MeV to 50 MeV with a power up to 500 kW. The beam electrons are to be converted into photons by means of an electron-to-gamma converter with the purpose of inducing photonuclear reactions in a target to produce exotic isotopes. In the process of conversion, the primary electron beam power deposition in the converter causes a significant increase of the temperature that must be dissipated.

The converter performance contributes notably to the overall isotope production and extraction efficiency. This thesis describes the work to optimize and verify the conceptual design of the electron-to-gamma converter through simulations and experimental measurements.

Contents

List of Tables

List of Figures

ACKNOWLEDGEMENTS

I would like to thank:

my husband and my family, for always supporting me.

Dr Dean Karlen for support, and mentoring,

Dr Alexander Gottberg for encouragement, and patience.

Paul Birney, Mark Lenckowski, Paul Poffenberger,

the TRIUMF machine shop personal

and the TRIUMF vacuum group for supplying the means to experiment.

University of Victoria, for funding me with a Scholarship.

TRIUMF for support.

DEDICATION

To Whom It May Concern

Chapter 1

Introduction

The Advanced Rare IsotopE Laboratory (ARIEL) is a major new facility under construction at TRIUMF, the Canadian Laboratory for particle and nuclear physics. The objective of ARIEL is to expand the Rare Isotope Beam (RIB) production of the laboratory by developing two new target stations: the ARIEL Electron Target East (AETE) and the ARIEL Proton Target West (APTW).

The isotopes produced by ARIEL will be used for materials science research, nuclear physics and astrophysics investigations, medical and biological applications, and fundamental symmetry research.

To produce short-lived rare isotopes ARIEL will use proton-induced spallation, fragmentation and fission in the APTW, and electron-driven photonuclear reactions in the AETE, and will use the Isotope Separation On-Line (ISOL) technique. With the ISOL method the reaction products are quickly extracted from a thick target, ionized and accelerated to form an ion beam that is mass analyzed and delivered to experiments.

The main photonuclear reaction used at the AETE is photofission, which splits ^{238}U into a few fragments, thereby producing a narrower set of neutron rich isotopes, with less isobaric contamination, as compared to those produced in proton induced fission reactions. As a consequence, this simplifies isotope separation and by reducing target area activation, simplifies issues related to remote handling.

A disadvantage of photofission is that the fission yield per electron is considerably lower than per proton, however, one can attempt to compensate this by increasing the electron beam flux [21].

To produce photons, the AETE uses an electron-to-gamma converter. This device not only provides high energy Bremsstrahlung photons but it also absorbs power from primary and secondary electrons thereby reducing the heat load on the sensitive target material. The electron-to-gamma converter concept design consists of a high-Z metal layer bonded to a low-Z metal customized to function as a heat sink and as an absorber for primary electrons passing through the high-Z layer (Fig. 1.1).

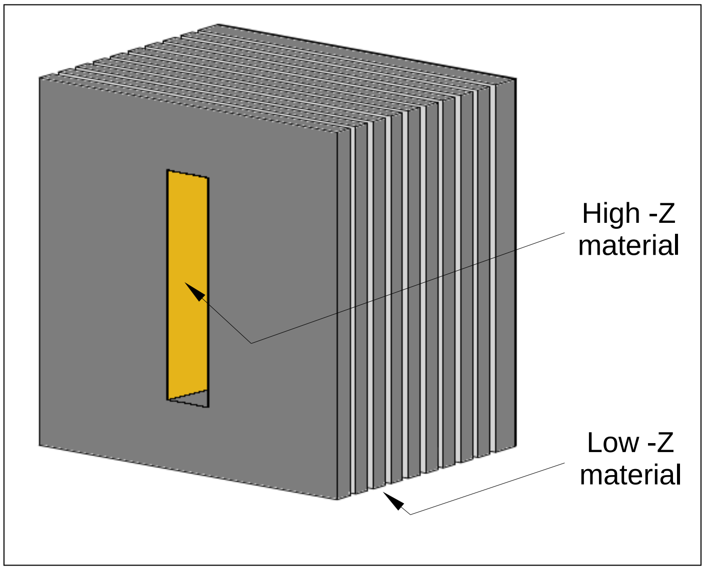

Figure 1.1: Converter concept design.

The main goal of this thesis is to verify, by means of simulations, that the current parameters of the converter design allows a sufficient gamma production to induce an isotope production rate of 10^{10} $(\mathrm{kWs})^{-1}$ while minimizing the power absorbed by the target. Through this thesis isotope production refers to those isotopes in the fission region with neutron numbers between 30 and 100.

To verify the photon and isotope production, as well as the power absorption, a program using Geant4 [3] was developed. A complementary study of the thermal response of the converter was performed with COMSOL Multiphysics [2], along with an experiment for obtaining the heat transfer coefficient of the converter heat sink.

For this project, high thermal contact cladding technologies were identified and coating companies were contacted to acquire samples with the characteristics that match the high-Z metal layer junction of the converter. Also a test to irradiate those samples was designed in order to determine which coating has the best adhesion. To irradiate the samples, a vacuum test chamber was assembled and installed at the end of the 300 keV e-linac Electron Low energy Beam Dump (ELBD) section.

The physics that drive the design of the converter are described in Chapter 2, along with a verification study of the design parameters of the converter. Chapter 2 also describes the cladding techniques and potential machining methods to produce the converter.

Chapter 3 presents a numerical study of the photon flux and isotope production rates with four different models of the converter. Also, the power absorbed by the converter models is given in this chapter with a thermal analysis based on the results of the power absorption study.

Chapter 4 describes a vacuum system assembled for testing samples coated with the cladding techniques chosen in Chapter 2, and shows the results of microscopic examination of some of those samples. Also, this chapter describes the methodology, based on thermal simulations, to irradiate samples for testing their cladding bonds.

Chapter 5 presents the results of a preliminary test to obtain the heat transfer coefficient of the converter heat sink.

Conclusions are given in Chapter 6.

Chapter 2

Converter design

The initial AETE design is suitable for electron beam power up to 100 kW, for energies between 30 MeV and 50 MeV. The design includes a converter to produce gammas[1] in order to induce photonuclear reactions in the target with the purpose of producing exotic isotopes.

Irradiating directly a target with the AETE electron beam above 500 W would deposit an unsustainable power density into the metallic target container increasing its temperature and causing it to fail. On the other hand, high energy Bremsstrahlung photons produced when electrons strike the converter are capable to induce photonuclear reactions within the target, while imposing less power deposition density in the target container.

Bremsstrahlung radiation is produced when electrons passing through matter decelerate due the Coulomb fields of the material's atoms, causing the incident electrons to lose energy which is emitted in the form of photons [13]. The average energy loss during Bremsstrahlung emission by an electron of energy E, in a thickness of matter dx, can be approximated to

$$\left(-\frac{dE}{dx}\right) \approx 4\alpha r_e^2 N_0 E Z^2 \ln\left(-\frac{183}{Z^{1/3}}\right) \quad [25] \tag{2.1}$$

where α is the fine structure constant, E is the energy of the electron with radius r_e that impinges a medium with an atomic density N_0, and atomic number Z.

The probability to emit a Bremsstrahlung photon is given by the cross section of the process and is proportional to

---

[1] For this thesis, the terms photons and gammas are used interchangeably.

$$\sigma_{BrS} \propto \frac{e^2 Z^2 E}{m_e^2} \quad [25] \tag{2.2}$$

with e the charge of the electron, and m_e the mass of the electron. The converter should therefore be made from high-Z materials, and to obtain high energy Bremsstrahlung photons, the material should have high N_0.

Increasing the energy of the electron E increases the probability of the emission of Bremsstrahlung photons linearly, increases the energies of the Bremsstrahlung photons, and decreases the angle over which the photons are emitted [13]. However, not all photons are capable of inducing photonuclear reactions in a target. Here, those photons that induce photonuclear reactions are called effective photons. The energy range of effective photons for the fission of ^{238}U goes from 3 to 30 MeV [22], [Appendix A].

Results of Geant4 [3] simulations of 10^7 electrons performed to obtain the photon flux, the effective photon flux and the isotope production are presented in this chapter. Further description of Geant4 is presented in chapter 3.

Figure 2.1 shows the Bremsstrahlung flux of photons passing through the nominal target container volume of 56.5 cm^3 for different electron beam energies hitting the converter (fig. 1.1).

The characteristic shape of the Bremsstrahlung photon spectrum is shown in figure 2.1. At low energies the flux is determined by the energy levels of the most tightly bound electrons. Starting at 100 keV the plots show the absorption edges of gold. At 511 keV there is a peak corresponding to the positron annihilation energy. Finally, the energy cut off for each curve occurs at $h\nu = E$.

Figure 2.2 shows the flux of effective photons passing through a target container volume of 56.5 cm^3 as a function of electron beam energy for a fixed beam power. The power of the beam is fixed because, ultimately, the isotope production is limited by the power deposited in the converter and in the target. The effective photon flux dramatically increases from 5 to 20 MeV, then increases at a lower rate until reaching a maximum at 40 MeV followed by a decrease, this is because the primary electrons decrease at growing energy for a fixed beam power. Therefore, using energies above 40 MeV does not improve the effective photon production and so would not increase the rate of isotope production. Thus, an energy range from 30 to 40 MeV is desirable to use in ARIEL.

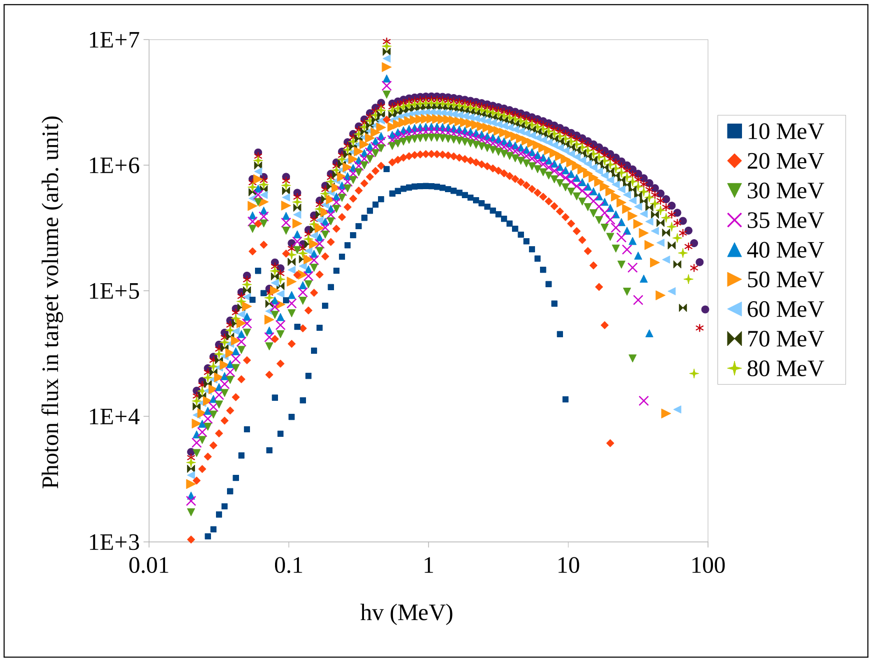

Figure 2.1: Photon flux in bins of the log of the photon energy.

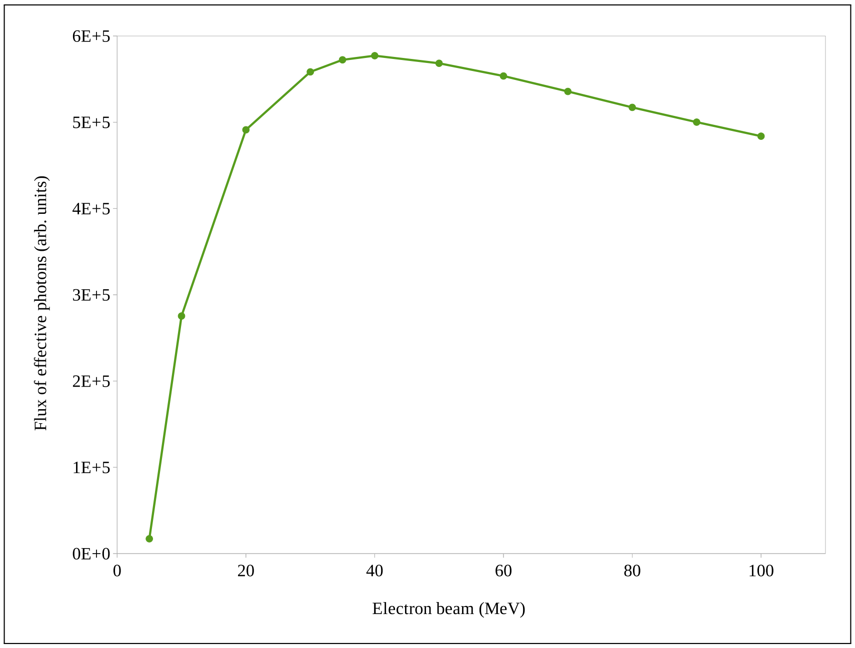

Figure 2.2: Flux of effective photon as a function of electron beam energy for a fixed beam power.

The high energy photons must reach the target downstream in order for the photofission process to take place. The dominant interaction process for photons with energy above 1 MeV is pair production, the creation of an electron and a positron [23]. The probability of this process to happen is given by

$$\sigma \sim Z^2 \log E_\gamma \quad [5] \tag{2.3}$$

where E_γ is the energy of the photon. Therefore parts downstream of the high-Z converter should be made from low Z materials, where possible.

2.1 AETE e-to-γ Converter

The conceptual design of the ARIEL e-to-γ converter (Fig. 2.3) consists of two main parts, a high-Z metallic coating (trench coating) to convert the beam electrons into photons, and a low-Z fin system to dissipate the heat from the metallic coating and to absorb surplus beam electrons and electrons from pair production. Another feature under consideration is a back coating to stop electrons that happen to pass through the trench coating and the fins. The electron beam will be rastered to distribute the beam power uniformly across the trench.

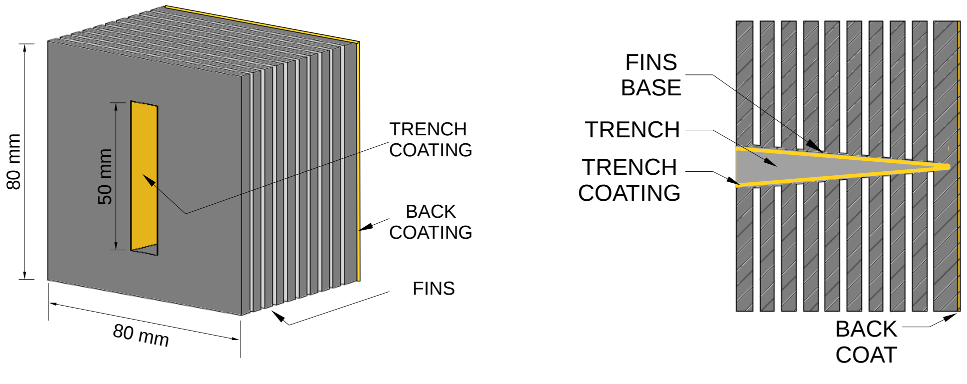

(a) Converter isometric view

(b) Converter trench view

Figure 2.3: Converter concept model. (a) Isometric view of the converter, (b) top view of the converter cutaway to expose the coated trench.

2.2 Converter materials

To fulfill the essential function of the converter, that is to produce photons from electrons, the material of the trench coating should have a high atomic number since the probability of producing Bremsstrahlung photons is proportional to the square of the number of protons Z (Eq. 2.2). Also, as the photon production inevitably causes a thermal load, the materials of the converter should effectively dissipate the heat and it should reduce the thermal load on the target and its container. Therefore, the materials to use on the converter should have good thermal conductivity and possibly a high melting point. High-Z metallic elements with high melting point, good thermal conductivity, and good machinability are good candidates to be used on the converter coating. Among the metals with atomic numbers between 73 and 92, tantalum with 73 protons, tungsten with 74 and gold with 79 are good options for the converter trench coating due to their mechanical-thermal properties and to their commercial availability.

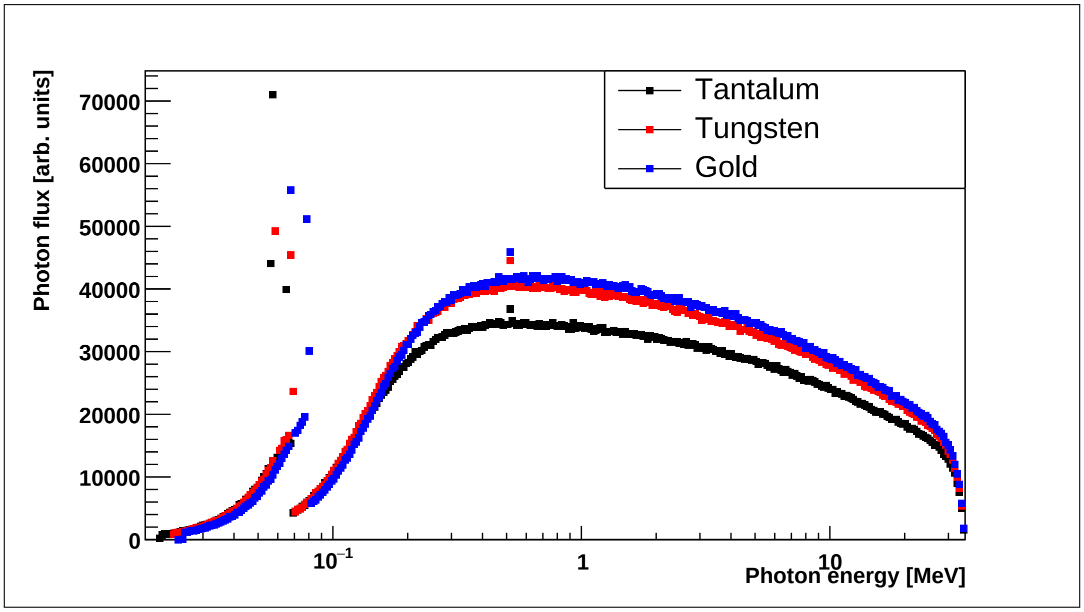

Figure 2.4: Bremsstrahlung flux from 35 MeV electrons striking a 0.5 mm thick coating of tantalum, tungsten, or gold.

Simulations of electrons of 35 MeV striking a plate of 0.5 mm thick of tantalum, tungsten and gold were performed in order to compare their photon production. From the resulting photon flux (Fig 2.4) it can be seen that the tantalum has the lowest photon production, and that the difference in the photon production of the W and Au is small, so, based on this comparison either of these two metals can be used to coat the converter.

The converter is designed to transfer heat from the trench coating to its fins which is subsequently dissipated to water circulating through the fin system. The fin system of the converter needs to be made from a material with excellent heat conductivity, a reasonably high melting point, and easy machining, but more importantly, the material must not absorb a large fraction of the photons produced in the trench coating.

Table 2.1 shows the melting point and thermal conductivity of aluminum and cooper, two widely used metals for thermal applications. Copper has better thermal properties than aluminum, however, copper has a larger atomic number which according to equation 2.3 would increase the pair production probability, hence aluminum is the best option to produce the converter heat sink.

Metal	**Atomic number**	**Melting point**[18] **(°C)**	**Thermal conductivity**[11] **(W/ m· C°)**
Al	13	660.3	205
Cu	29	1084.6	401

Table 2.1: Atomic number, melting point and thermal conductivity of metals considered to be used in the converter heat sink production.

Due to the heat conduction path, there needs to be high quality bonding between the coating and the fins. Also, to reduce stress at high temperature, the thermal expansion coefficient of the metals of the converter coating and the fin system should be similar.

Compared to tantalum and tungsten, gold is the best candidate to coat the trench of the fin system since it has the closer thermal expansion coefficient to that of aluminum (see table 2.2). Also, note that gold has the highest thermal conductivity of the metals considered for coating.

Metal	**Thermal expansion coefficient**[10] $(\mathbf{10^{-6}/C^{\circ}})$	**Thermal conductivity**[11] $(\mathbf{W/m \cdot C^{\circ}})$
Al	22.2	205
Au	14.2	314
Ta	6.5	57.7
W	4.3	173

Table 2.2: Thermal expansion coefficient and thermal conductivity of the metals considered to use in the converter production.

2.3 Converter geometry

While a simple foil of high-Z metal can convert electrons to photons, it cannot solve the problem of restricting the target container exposure to a primary beam power of 25 kW [16]. Furthermore, the beam power would have to be limited to low levels to prevent damage to the foil since it would not have sufficient cooling.

The proposed converter geometry solves both of these problems. The design consists of two surfaces positioned at a large angle with respect to the beam to form a “V” that reduces the power density of the beam on the metal surface and significantly increases the area available for heat dissipation.

It is important to minimize the distance between the converter and target, to maximize the photon flux in the target. While the large angle orientation of the converter surface works against that, it does allow an effective heat dissipation system to be implemented. Note also that the large angle increases the effective thickness (fig. 2.5) traversed by the beam electrons.

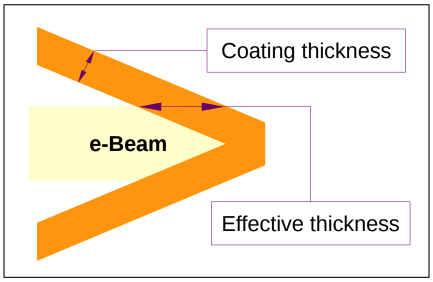

Figure 2.5: Effective thickness of the trench coating.

2.4 Converter coating thickness

The optimal thickness of the metal to produce photons depends on the electron stopping power of the material at a given electron beam energy. An optimum thickness produces a large flux of effective photons while minimizing their absorption in that layer.

The nominal design of the trench of the converter has a depth of 54.5 mm and an aperture of 11.4 mm (figure 2.6 a). With this aperture the angle that each of the two sheets of high-Z material would have with respect to the electron beam direction is 5°.

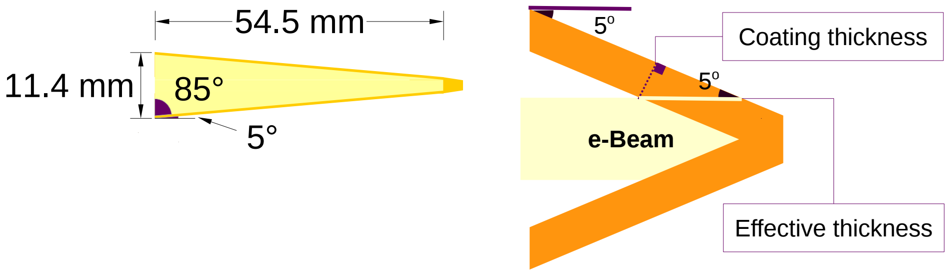

(a) Trench dimensions (b) Effective thickness

Figure 2.6: Trench coating sketch. (a) the trench coating dimensions, (b) the effective thickness and its geometrical relations with the coating thickness.

With t_{coat} as the coating thickness, t_{effe} as the effective thickness and θ the angle of the coating sheet with respect to the beam direction the effective thickness as a function of coating thickness can be obtained with equation 2.4.

$$t_{effe} = \frac{t_{coat}}{\sin\theta} \tag{2.4}$$

The effective thickness corresponding to coatings of various thicknesses taking into consideration the 5° angle as well as the corresponding fraction of stopping range S_o is shown in the table 2.3.

Coating thickness (mm)	**Effective thickness (mm)**	**S_o fraction** [19]
0.06	0.695	0.1
0.1	1.158	0.2
0.2	2.317	0.4
0.3	3.475	0.5
0.4	4.633	0.7
0.5	5.792	0.9
0.6	6.517	1.0

Table 2.3: Gold layer thickness and the effective thickness (path length for beam electrons), and fraction of stopping range, S_o.

The stopping range of 35 MeV electrons in a gold sheet in the continuous slowing down approximation (CSDA) is S_0 6.517 mm [19].

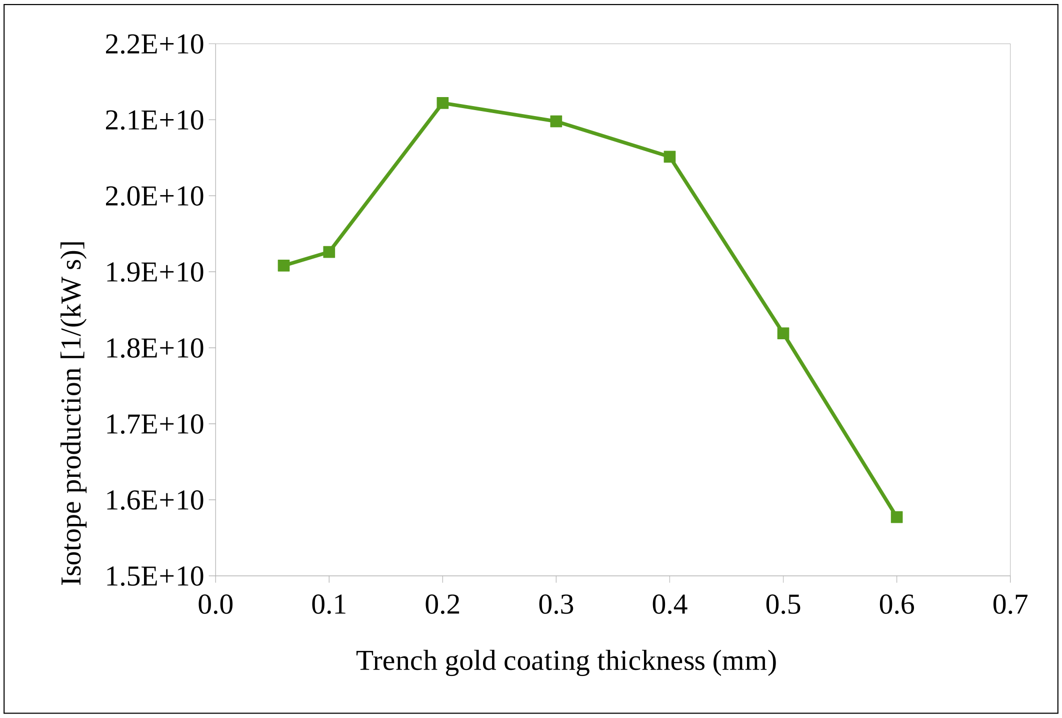

Figure 2.7: Isotope production as a function of trench gold coating thickness. The maximum production rate of isotopes is obtained when the gold coating is between 0.2 and 0.4 mm thick.

Simulations of electrons striking the converter using the thicknesses of the gold coating shown in the table (2.3) indicated that a gold coating with a thickness between 0.2 mm and 0.4 mm would give the highest isotope production rate 2.7. This range of coating thickness corresponds to an effective thickness range of 2.317 to 4.633 mm.

2.4.1 Converter trench aperture

Figure 2.8 shows the converter trench aperture, which must be matched to the geometry of the target immediately downstream. The larger the aperture the wider the area of photons at the target location.

Different aperture angles were simulated with an electron beam of 35 MeV. For each angle simulated, the coating thickness was adjusted to maintain the optimal effective thickness, 2.3 mm.

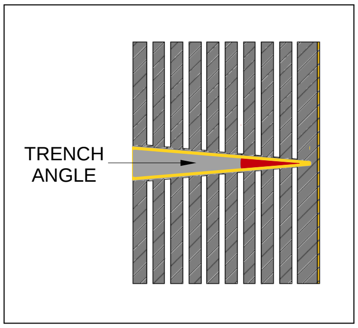

Figure 2.8: Trench aperture angle.

Figure 2.9 shows the isotope production tendency of the converter depending on the angle of the aperture of the converter trench. An angle of aperture of 10° gives the highest isotope production of 2.1×10^{10}/kWs. The extreme limit of the aperture is a gold plate perpendicular to the beam with an aluminum base to dissipate heat. The isotope production of a gold plate is 1.4×10^{10}/kWs, which is about 65% less than the isotope production obtained of the converter with an aperture of 10°.

Figure 2.9: Isotope production of a converter with different trench apertures with a fixed effective thickness of the converter coating.

2.5 Cladding technologies

There are many techniques to coat surfaces, however for the required coating thickness in the range of 0.1 to 0.3 mm, the options reduce to electroplating and explosion welding.

In electroplating a metallic coating is deposited on the cathode of an electrolytic cell. The components of the electrolytic cell are an anode, a cathode and an electrolytic solution that contains the metal ions for the coating. The deposition of the coating happens when a electric current flows in the electrolytic solution [14].

Explosion welding clads two metal pieces with a detonation that travels at supersonic velocity. A detonation wave causes a shock front that compresses and heats the surfaces, inducing the valence electrons to overcome the repulsive forces resulting in sharing of their orbits [8].

Commercially, electroplating is not done with a wide variety of metals and thickness, but companies can produce deposits of different thickness for special requests. On the other hand, explosion welding is an expensive technique, but with a wider variety of metals to bond and a broad range of thickness to choose from. Both cladding techniques have the limitation that they can only be applied on plane surfaces, narrow angles as the one that the trench holds are not available industrially.

2.6 Fin system machining

The trench aperture of the converter is too narrow to be coated with the thickness desired with any of the mentioned cladding technologies, so the fin system can not be machined from one aluminum block. There are two methods considered to construct the fin system of the converter: welding and bending.

2.6.1 Welding

The welding method builds the converter by joining a pair of identical fin systems each machined from an aluminum block. The alloy 6xxx series of aluminum have low alloy content and are easy for milling [9] that makes them a good option. Also this series is commercially available in blocks with suitable dimensions to produce each of the parts.

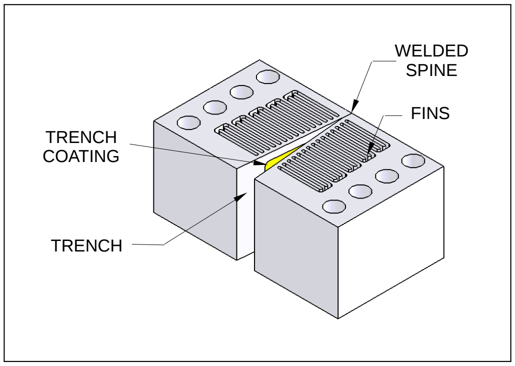

Figure 2.10: Welded converter conceptual design.

Once the fin system has been cut from an aluminum block with a water jet, gold coating would be applied on the plane surface of the fin system, after that, the two parts will be welded together 2.10.

A basic and widely used technique to weld is arc welding. Arc welding uses the heat produced by an electric arc to melt the materials and requires filler material between the metals that are to be joined. Specifically, the aluminum alloy 6061 is compatible with the filler alloy 4043 and are suggested to be used for elevated temperature applications [9]. However, this technique is difficult to implement on zones that are not deep such as the converter spine (see figure 2.10). So, an alternative welding technique considered to use is electrom beam (EB) welding, to heat up the metals to weld. EB weldings are vacuum proof, do not require surface preparation nor filler. EB welding gives narrow welds and can weld pieces of aluminum up to 500 mm depth [17].

2.6.2 Bending

The bending method would start by cutting fins on one side of a thick aluminum plate, then on the other surface, a gold coating would be applied, and finally the part would be bent in half (Figure 2.11). This model has more fins than the welding converter but they are thinner and shorter [2].

The problem with the bending method is that the aluminum to coat has to allow for a small bend radius. The aluminum of the 5xxx series has a suitable bend radius, however, the required thickness is not widely commercially available.

Another issue with this method is that the coating can be damaged when the part is bent. The machines used to bend usually has to be in contact to the whole area that is subjected to bending, particularly to the surface corresponding to the direction of the V junction of bending. Hence, the surface of coating can be damaged in the process.

It is important to have a uniform surface at the V junction of the converter, but this area can easily shrink if the bending method is applied. The resulting wrinkles in the gold layer could increase the effective thickness of the coating beyond the optimal range (2 to 3.5 mm).

The V junction of the converter is paramount, because it is the closest coating to the target so that the electrons that have not been converted into photons have only 2.5 mm of aluminum to absorb its energy and not deposit it in the target. The average stopping distance in aluminum is 60.2 mm for 35 MeV electrons, thus a coating of a high-Z material behind the converter V junction could be highly favourable.

The V junction of the converter will be the hottest area of the converter due to the power density there, and if it does not dissipate heat efficiently the converter could fail. With the bending method the converter would be one piece and it would not

---

[2] Simulations of this model are not presented in this thesis

have a gap at the V junction. The strength of the bending converter would rely on the state of the aluminum after bending.

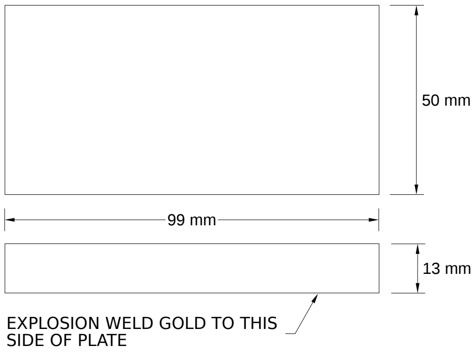

(a) Dimensions of the initial Aluminum plate

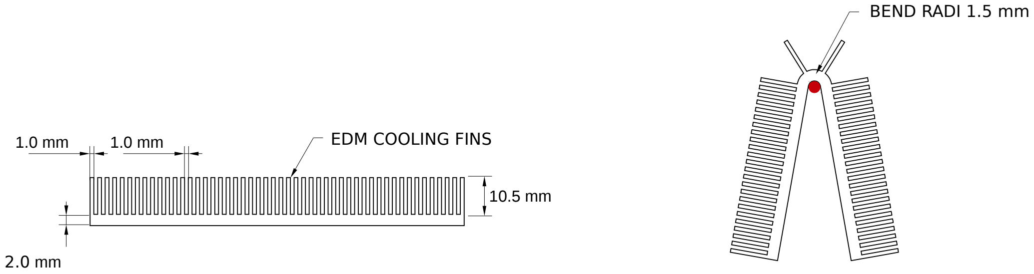

(b) Fins

(c) Final bent converter

Figure 2.11: Bent converter conceptual design.

Chapter 3

Numerical results

The programs used to perform the simulations of this project were Geant4 [3] and COMSOL [2] Multiphysics®.

COMSOL Multiphysics® is a software based on finite element analysis with multiple applications for Physics and Engineering. COMSOL was used for heat transfer simulations.

On the other hand, Geant4 is a free Monte Carlo based software written in the C++ object oriented programming language that simulates the passage of particles through matter.

Geant4 was used to obtain the energy of photons, isotope production rates, and total energy absorbed. In this thesis the simulations with this software correspond to 10^9 electrons requiring 15 days running time on a single CPU.

3.1 Photofission and isotope production

Four models of the welded design of the converter were simulated. The characteristics of each converter model are shown in the table 3.1

Model	Coating thickness (mm)	Aluminum base (mm)	Back coating[1]
A	0.2	0.7	Yes
B	0.2	0.7	No
C	0.2	2.0	Yes
D	0.5	0.7	Yes

Table 3.1: Characteristics of the converter models simulated.

The model A is the nominal model of the converter with a gold back coating, the optimum gold thickness of 0.2 mm and the minimum aluminum thickness base that is machinable of 0.7 mm (fig. 2.3 b). Model B is identical to A but without including the back coating, in order to verify the effectiveness of this part in reducing the power absorbed by the target. Model C has the optimal gold coating but has a thicker aluminum base that is easier to fabricate and is expected to have improved mechanical properties. Model D has the minimum aluminum base thickness and a larger than optimal gold thickness coating in order to investigate the tradeoff between isotope production rate and absorbed power on target.

The Bremsstrahlung photon production of each of the converter models was simulated with an electron beam of 35 MeV at 50 kW.

To simulate the isotope production, the target material composition of the AETE was implemented in the Geant4 code. The AETE target is composed of 52.83 at % ^{238}U, 0.159 at % ^{235}U, 46.51 at % ^{12}C, and 0.50 at % ^{13}C. Its density is 3.5 g/cm^3. The target shape is a cylinder of 40 mm diameter and 45 mm tall, giving a volume of 56.5 cm^3. The target is inside of a 0.5 mm thick cylindrical container made of tantalum. The front face of the target is situated 2 mm downstream of the converter (fig. 3.1).

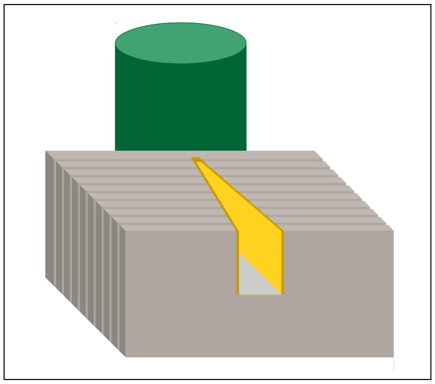

Figure 3.1: Sketch of the position of the target behind the converter cutaway.

The number of Bremsstrahlung photons in the simulations of 10^9 beam electrons were scaled to estimate the rate of isotopes produced corresponding to the 35 MeV, 50 kW electron beam of the AETE. The results are shown in table 3.2. Figure 3.2 shows the converter model A projected yield of isotopes from photofission in the

---

[1] The back coating is a gold coating with a fixed thickness of 0.6 mm

regions of interest of isotopes with 30 to 100 neutrons, the colour scale shows the yield per kW· s. The shape of the projected yield of isotopes for the other converter models is similar to the one presented.

Converter	**Effective Photons on Target**		**Isotope Production**
model	Number (10^{14}/kW·s)	Mean Energy (MeV)	**10^{10}/kW·s**
A	1.75	7.23	2.1
B	1.79	7.33	2.2
C	1.74	7.23	2.1
D	1.64	6.89	1.8

Table 3.2: Isotope production rate.

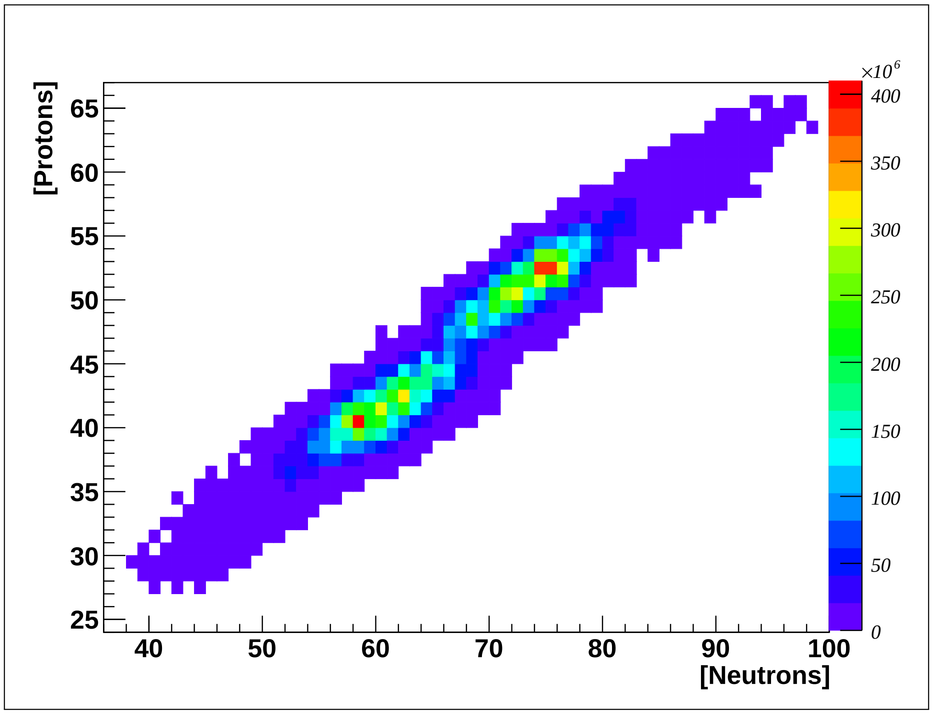

Figure 3.2: Isotope production for the converter model A with a gold coating of 0.2 mm, and an aluminum base of 0.7 mm. The colour scale shows the yield per (kW s)

As expected, matching with the photon production, the converter model D was the one with the smallest isotope production since it does not have the optimal coating thickness. The converter model C with the optimal gold coating thickness but with a thicker aluminum base has a slightly higher isotope production than converter model D. The converter model A has a higher isotope production than the model D because of its optimal gold coating thickness and its minimum base thickness. The highest isotope production belongs to the converter model B, that has the optimal coating thickness and minimum aluminum base but does not have the back coating. Since, the isotope production of the four models is similar, other factors should be taken into account, such as power absorption, durability and cost of production.

3.2 Energy and power absorbed

The power absorbed from electrons and photons passing through the parts of the converter, the target, and the target container corresponding to each of the converter models is shown in the table 3.3. This power is only due to particles passing through matter and does not take into account conduction or convection, therefore the water has low power absorbed registered in this simulations.

Component	**Fraction of beam power absorbed**			
	A	B	C	D
Trench coating	0.21	0.21	0.21	0.42
Fin system	0.19	0.19	0.21	0.11
Water	0.02	0.02	0.01	0.01
Back coating	0.04	0.00	0.04	0.02
Container	0.01	0.01	0.01	0.01
Target	0.25	0.28	0.24	0.16

Table 3.3: Power absorption for converter model A, with 0.2 mm thick gold coating and an aluminum base of 0.7 mm thick. Fraction of the beam power absorbed by each of the parts that compose the converter, the target and the target container.

The converter model A with a trench coating of 0.2 mm absorbs 21% of the beam power in the trench, and the target absorbs 25% of the beam power.

For the converter model B of 0.2 mm thick gold trench coating and 0.7 mm thick aluminum base without back coating the power absorbed by the target container and the target is higher than the converter A with the back coating. Therefore, the back coating is beneficial for the integrity of the target.

From the initial e-beam power, 21% of the power is absorbed by the trench coating of the converter model C with the thicker aluminum base of 2 mm, and a trench coating of 0.2 mm thickness, with this converter model the container absorbs 1% and the target 24%, which is slightly lower than the power absorbed by the converter model A.

The converter model D with a 0.5 mm thick trench coating and 0.7 mm thick aluminum base absorbed 56% of the beam power, leaving 1% of the beam power to be absorbed by the container, and 16% by the target. The whole system absorbed 70% of the initial power.

Each converter-target assembly design absorbs approximately 72% of the electron beam power, the rest of the power is carried away by photons and other particles exiting the system. Figure 3.3 compares the power absorbed by the components of the system corresponding to each converter. The converter model D with 0.5 mm gold coating and 0.7 mm aluminum base has the lower power absorption except for the trench coating and also has the lowest isotope production of the four models. This behaviour is beneficial for the target integrity, however, the high power absorbed by the trench complicates the production of the converter. In contrast, the converter model B that does not have a back coating and has a 0.2 mm thick gold coating in the trench yields the highest isotope production but it also allows the highest power absorption on the target.

Table 3.4 shows the comparison of the ratio of beam power absorbed by the target to isotope production of the four converter models. The aim is to have a high isotope production with the minimum power absorbed by the target, so the smallest ratio shows the optimal converter model. The converter model with the smallest ratio is the model D, however this one has the largest power absorption in the trench. The next preferable models are the A and the C, however the model C due to its thicker aluminum base that makes easier its machining is preferable than the model A that has an aluminum base of 0.7 mm.

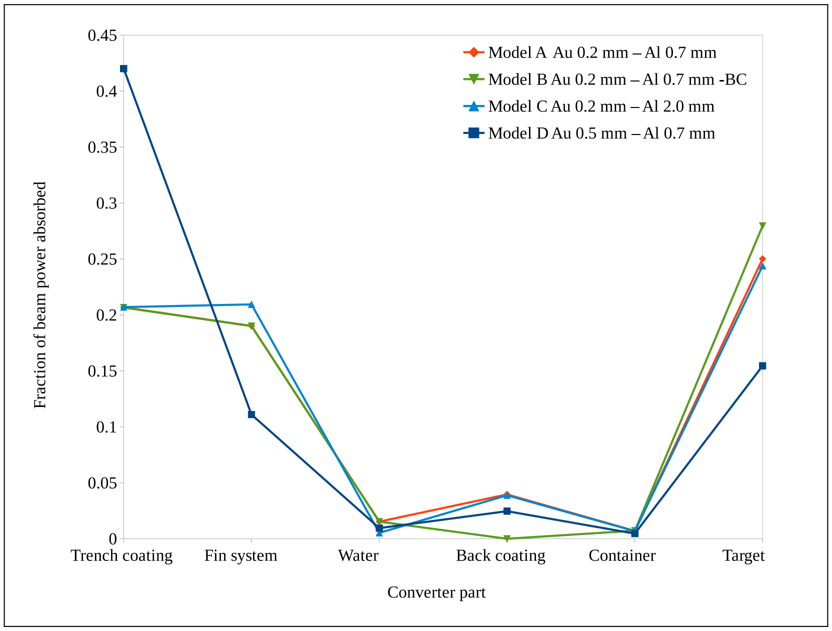

Figure 3.3: Power absorbed by the parts of the different converter models, the container and the target.

Converter model	Ratio [10^{-11}kW s]
A	1.2
B	1.3
C	1.2
D	0.8

Table 3.4: Ratio of beam power absorbed by target to isotope production rate.

3.3 Temperature profile

The numerical modelling of temperature profiles of the converter models A, C and D was performed with COMSOL. The converter model B that does not have the back coating was not simulated because its fraction of beam power absorbed was similar to that of converter model A. The power absorption results from Geant4 simulations were used as heat sources for the converter in the thermal simulations, which consists of a stationary analysis where the boundary conditions fixed the water velocity and the initial temperatures of the converter and the water. The interface chosen was the Non-Isothermal Flow with a laminar approach, this solved the Navier-Stokes equations and the heat transfer equations simultaneously [4].

The mass flow rate required of coolant was determined assuming a maximum temperature difference between the inlet and outlet temperature of the water cooling of $\Delta T = 30°\text{C}$ with:

$$\dot{m} = \frac{\dot{q}}{c_p \Delta T}, \tag{3.1}$$

where $\dot{q}$ is the power to dissipate, and c_p is the specific heat of the cooling fluid, which is 4.178 $kJ/kg \cdot K$ for water at $T = 30°\text{C}$.

With $\dot{m}$, the flow velocity of the water cooling can be obtained by means of the equation 3.2

$$V = \frac{\dot{m}}{\rho A_c}, \tag{3.2}$$

where ρ is the density of the water, and A_c is the total area of the transverse section normal to the flux direction of the channels, which is $1.3{\times}10^{-3}$ m^2. Table 3.5 shows the velocity required to dissipate various power values.

q̇ (kW)	**ṁ (kg/s)**	**V (m/s)**
50	0.40	0.31
40	0.32	0.25
30	0.24	0.18
20	0.16	0.12
10	0.08	0.06

Table 3.5: Minimum flow velocities to extract different powers

Table 3.6 presents the maximum temperatures reached by each of the converter models when using the slower water velocity, 0.06 m/s.

Converter			**Maximum temperature (°C)**
Model	Au Coating (mm)	Al Base (mm)	
A	0.5	0.7	391.6
C	0.2	0.7	366.1
D	0.2	2.0	353.9

Table 3.6: Maximum temperature of the three converter models at the steady state. The beam power is 50 kW and the water flow rate is 0.06 m/s.

The melting temperature of aluminum is 660° C, and the gold melting point is 1064°C, so the maximum temperature from the simulations shows that both metals are well below their melting points. The heat maps of the converter model C (0.2 mm thick gold coating and 2.0 mm aluminum base) are shown in figure 3.4 and 3.5 for two different flow rates. The fresh water enters from the top of the converter and exits hot from the bottom.The power absorbed by the trench of this converter is 10.35 kW, and the fins absorbed 10.47 kW. According to the maps 3.4, the hottest area is the trench spine. This is because the tip of the converter trench coating is encrusted in a thicker fin which contacts water only on one surface unlike the rest of the central fins. On the map 3.4 (e) and (f) it is seen that the first fin also has a higher temperature for the same reason.

The maximum temperatures of the converter models at the steady state corresponding to different velocities are shown in the figure 3.6. The maximum temperatures at the steady state of the water cooling corresponding to each converter model are shown in figure 3.7. Note that the water is boiling for all the water velocities. The water that has a temperature above 100° is located in the hotter surfaces near to the spine of the converters, this is not convenient for the system because the boiling water near that surface would create an insulation layer that will not allow the dissipation of heat in that critical area and it will increase its chances of failing.

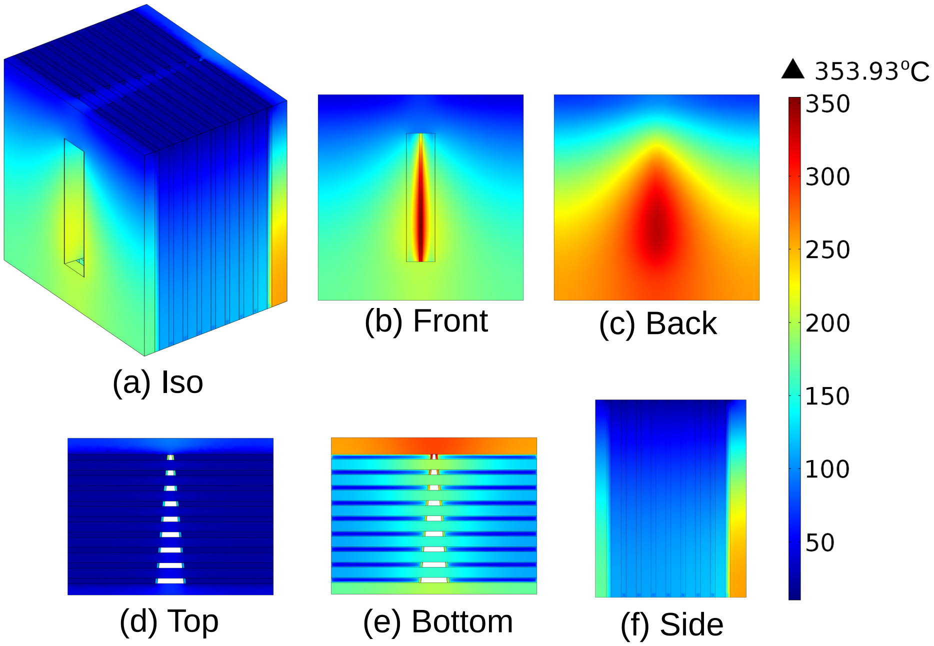

Figure 3.4: Temperature map of the converter model C using a water velocity of 0.06 m/s. Fresh water enters from the top and exits hot from the bottom.

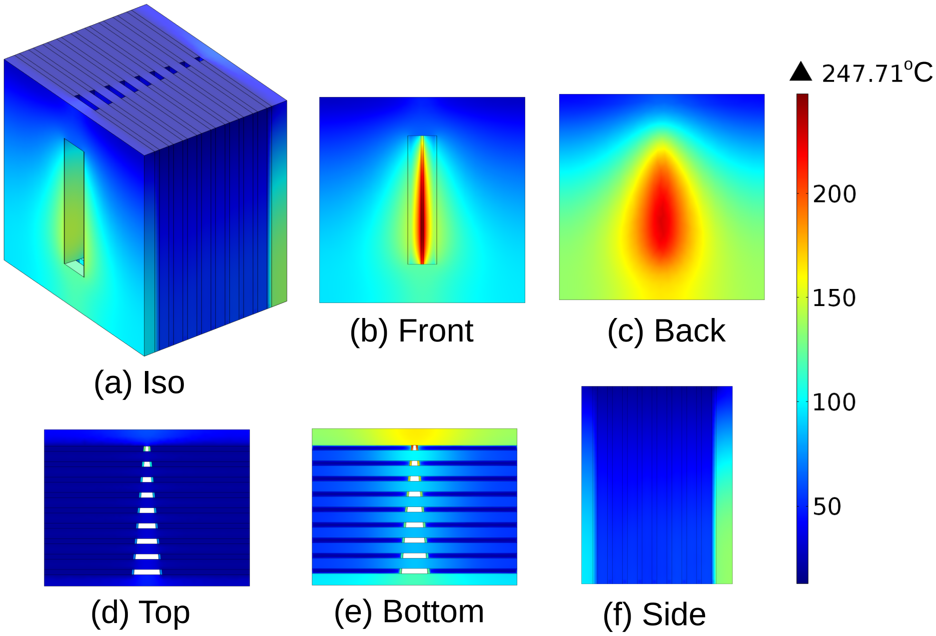

Figure 3.5: Temperature map of the converter model C using a water velocity of 0.31 m/s. Fresh water enters from the top and exits hot from the bottom.

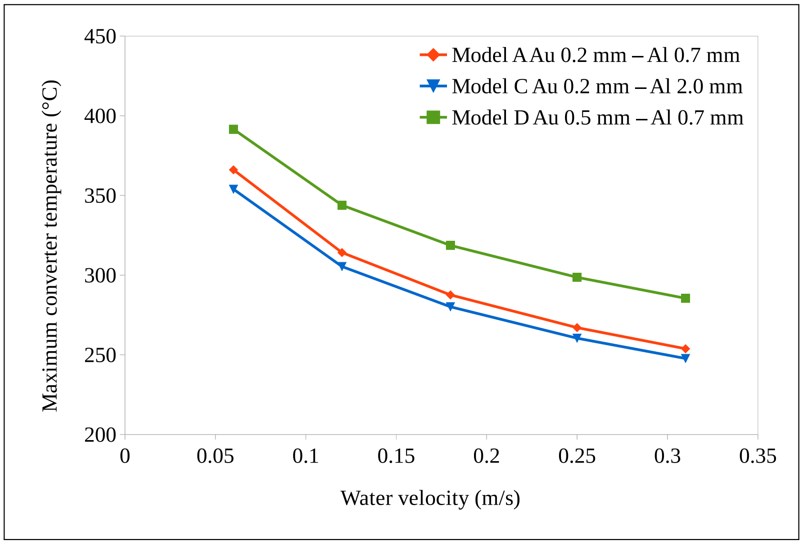

Figure 3.6: Maximum temperature at the steady state of the converter models corresponding to different water velocities.

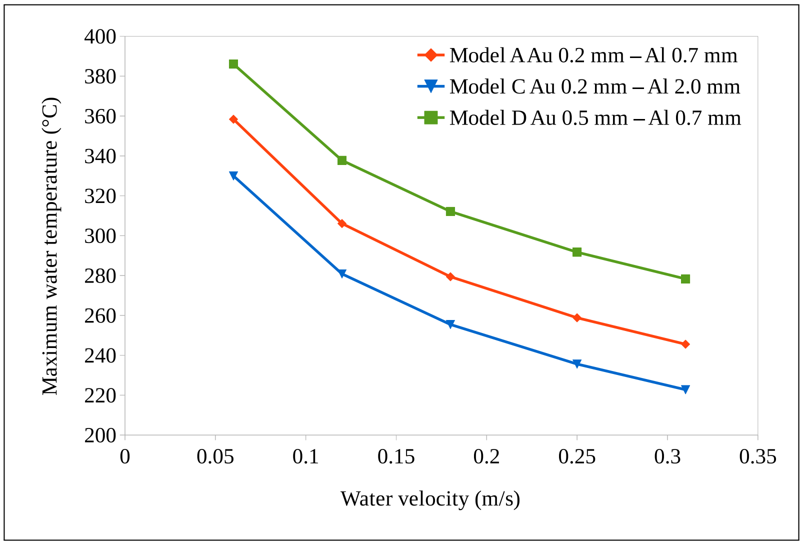

Figure 3.7: Maximum temperature at the steady state of the cooling water of the converter models corresponding to different flow velocities.

According to COMSOL simulations for the converter model C, with a flow velocity of 4 m/s, the water does not boil (figure 3.8). The converter model D which has the highest power absorption needs a flow velocity of 8 m/s to not have boiling water ($T_{water} = 98°$). Both water velocities far exceed the minimum water flow velocity predicted to dissipate 50 kW (see table 3.5)and while 4 m/s is achievable (W. Richert, personal communication, 2016), this velocity corresponds to a mass flow rate of 5.2 kg/s for the converter which is high for the entire flow loop and for the converter itself. Also, 2 m/s is the maximum recommended velocity to avoid erosion-corrosion on aluminum[15].

Furthermore, the temperature of the exiting water is too high for the flow loop and to reduce it, the flow velocity has to be even larger. Therefore, the fin system of the converter has to be studied further and modified accordingly. Decreasing the width of the channels and increasing the number of them could improve the system. Also, a thicker aluminum base could contribute to reduce the temperature of the cooling water. If it is possible to dramatically reduce the water velocity, the converter model D will be the optimal since it gives the largest ratio between the isotope production and the power absorbed by the target. If the fin system optimization does not significantly reduce the water velocity required then the converter model C will be the optimized converter model. For now, converter model C is selected as the nominal design.

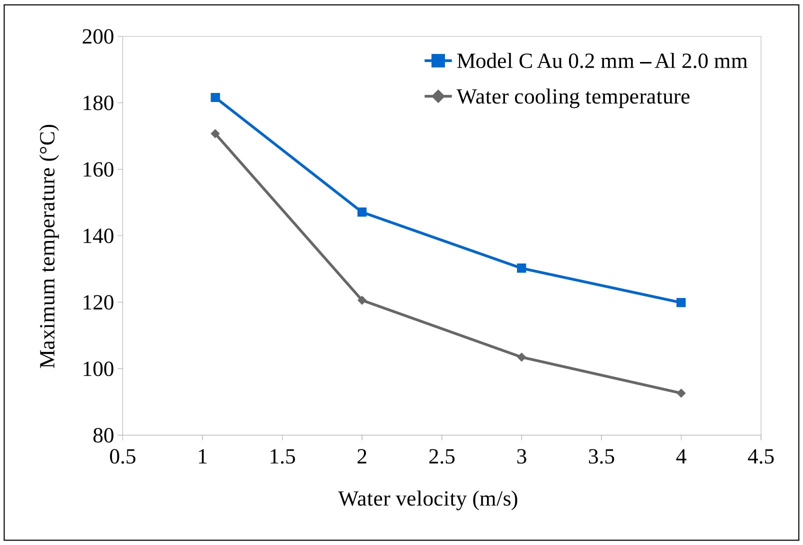

Figure 3.8: Maximum temperature at the steady state of converter model C and its water cooling, corresponding to different water velocities.

Chapter 4

Converter cladding test

As described in Chapter 2, there are two cladding techniques that are under consideration for bonding the gold layer to the aluminum structure, namely electroplating and explosion welding. In order to identify which cladding technique has better adhesion and durability, systematic tests will be performed before building the converter. For this purpose a converter irradiation test stand was assembled following strict vacuum and operational accelerator procedures.

4.1 Converter test stand

The converter test stand is installed at the e-linac Electron Low energy Beam Dump (ELBD) situated in the e-hall at TRIUMF.

The converter test stand consists of a UHV DN160CF 6-way cross coupled to the 300 keV electron beam through a gate valve to flange A (see figure 4.1 (b)). Flange B in figure 4.1 (b) has a Faraday Cup to measure the beam current when no sample is inserted and monitor the current that happens to pass through the sample under test.

A turbo molecular pump is connected to flange C. To monitor the vacuum pressure a convectron gauge and an ion gauge are installed in flange D.

Flange F has a borosilicate viewport to facilitate the alignment of the samples and to assist manipulations and diagnostics.

A sample holder is attached to a modified conflat flange (CF) full nipple on top of flange E. The CF full nipple has a 2 way liquid feedthrough for water cooling the samples.

To register the temperature of the samples, the CF full nipple has adapted up to six thermocouples on a feedthrough. Current flow through the sample is measured via a BNC feedthrough.

A motorized Z-stage with a bellow holds the CF full nipple allowing the sample holder (Figure 4.2) to move up and down. This feature allows any of the three samples to be inserted by remote control, as well as removing all to transmit the full beam to the Faraday cup. This eliminates the need to break the vacuum and enter the e-hall to change samples.

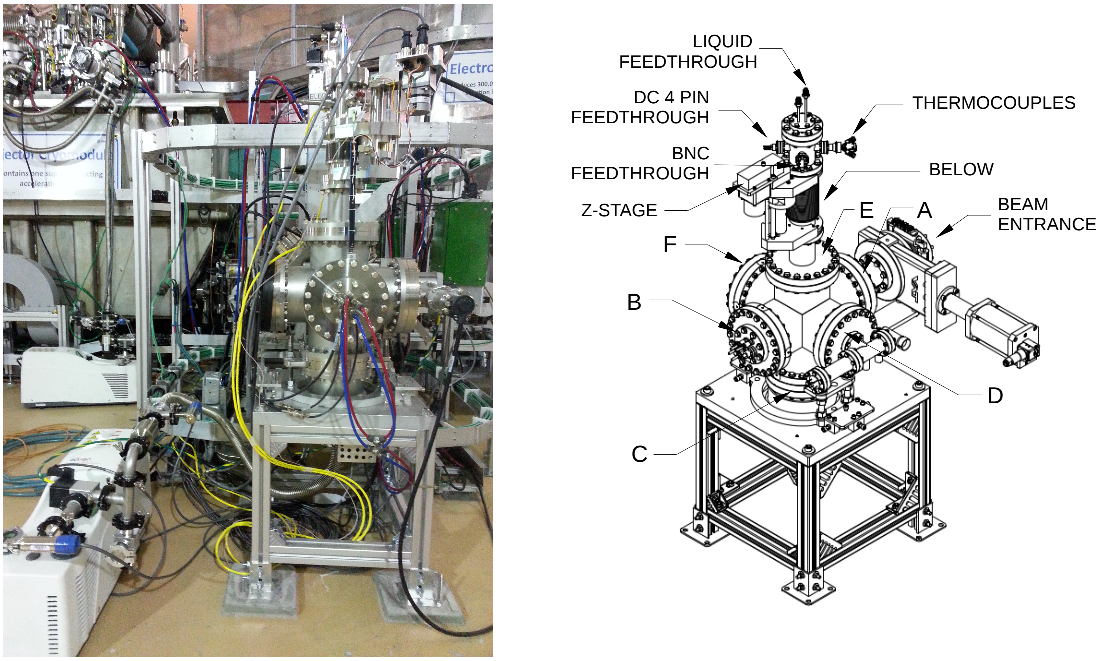

(a) Photograph

(b) Sketch

Figure 4.1: Converter test stand.

The sample holder (fig 4.2) consists of a copper U-shaped pipe attached to the liquid feedthrough connections with three pairs of brackets to hold cylindrical samples, the brackets embrace the pipe in order to transfer heat from the samples to the pipe and eventually to the water that flows in the pipe.

The brackets and the pipe are made out of copper since this metal has excellent thermal conductivity. The brackets are equally spaced and are capable of holding cylinders of a diameter up to 20 mm.

The sample holder is insulated from the chamber by means of a nylon double flange between the Z-stage and the cooling water feedthrough.

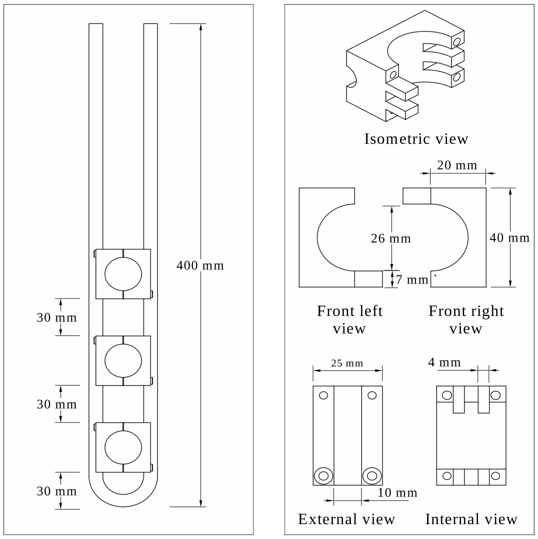

(a) Sample holder (b) Bracket

Figure 4.2: (a) Coper pipe for water cooling with three brackets. (b) Brackets composed of two parts.

4.2 Converter samples

The samples to test adhesion of coatings for the converter in the test stand consist of a heat sink part and a coating surface. The dimeter side of its coated area is limited to a maximum of 20 mm, and its height to a maximum of 25 mm, to ensure the sample fits in the sample holder.

Two cylinders of aluminum 6061 (figure 4.3) of 40 mm diameter and 40 mm height were electroplated with two different methods. The sample (a) was coated with a thin layer and the final gold thickness was approximately 0.01 mm.The method used to electro-coat the sample (b) consisted in applying gold coatings with subsequent polishing steps. This procedure was repeated successively until the gold layer thickness reached 0.5 mm. The two coatings are easily distinguished (figure 4.3).

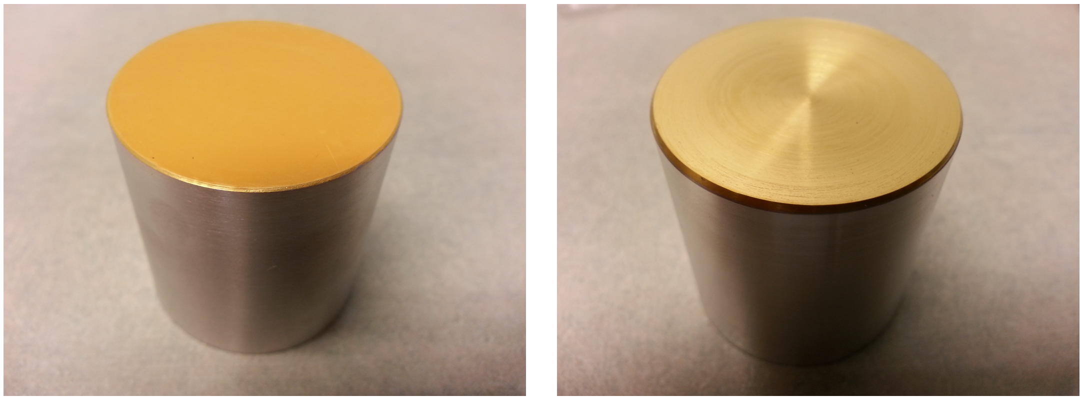

(a) Coating thickness 0.01 mm

(b) Coating thickness 0.5 mm

Figure 4.3: Samples with gold coating applied by electroplating.

From each cylinder three smaller cylinders of 16 mm diameter and 20 mm height were obtained and a 0.8 mm channel was drilled on each of them to have access to the back of the Au layer to add a thermocouple. The scrap pieces (figure 4.4) were used to examine the coating of the samples with a Scanning Electron Microscope (SEM) and a Focused Ion Beam (FIB).

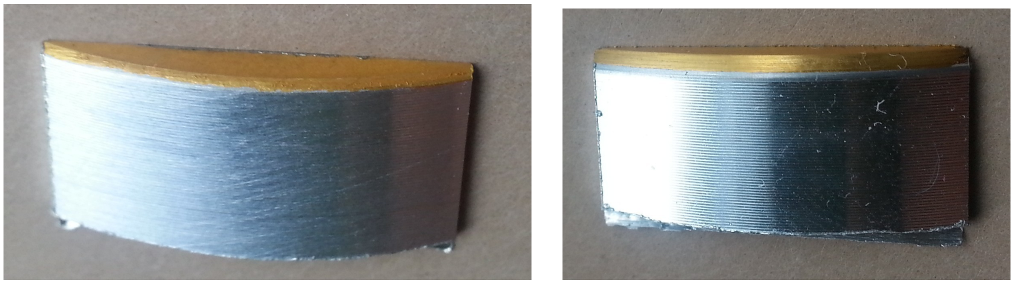

(a) Coating thickness 0.01 mm

(b) Coating thickness 0.5 mm

Figure 4.4: Scrap pieces of test aluminum cylinders used for examination with SEM and FIB.

4.2.1 SEM examination

With a scrap piece of each sample, a cross section was prepared for SEM examination. The procedure to prepare the cross section started with soaking each sample in an epoxy mixture. When the epoxy set, the samples were polished with sandpaper, starting with coarse paper and ending with fine diamond paper. The purpose of the preparation was to expose the bonding of the samples.

The SEM examination showed the initial condition of the two different coatings, and the thicknesses of the coating.

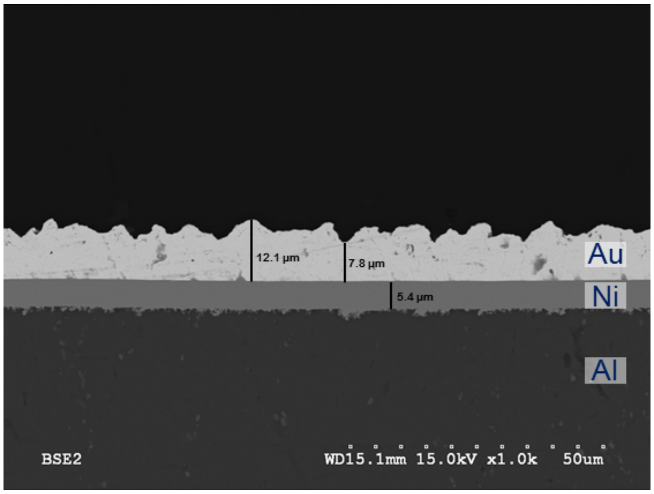

(a) Coating thickness 0.01 mm

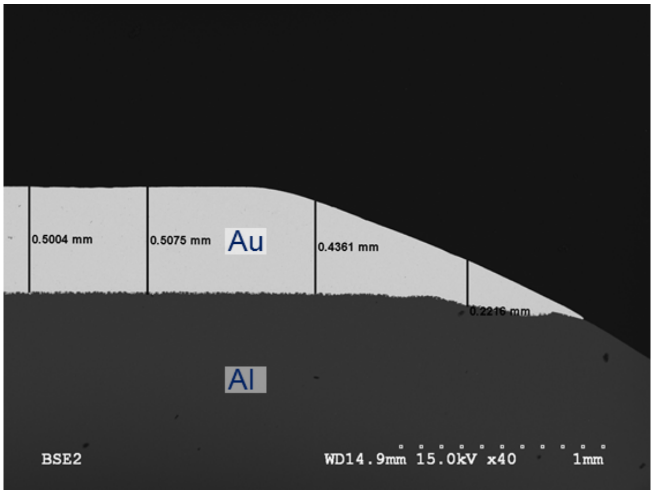

(b) Coating thickness 0.5 mm

Figure 4.5: Coating morphology SEM images, (a) the sample with the 0.01 mm thick gold coating has a precoating of nickel to improve the adhesion; (b) the sample with 0.5 mm thick gold coating does not have a pre-coating of Ni.

The sample shown in figure 4.5 (a) has a coating 0.01 mm thick, this thickness does not match with the thickness ordered of 0.1 mm. The SEM image in figure 4.5 (a) also shows the 0.005 mm thick nickel layer used to improve the adhesion of the gold coating and the aluminum. The nickel coating, exhibits penetration in the aluminum due to the roughness of the aluminum, however the gold coating does not appear to penetrate the nickel layer, which indicates polishing of the nickel layer.

The sample (b) on the figure 4.5 has a coating of 0.5 mm thickness as ordered, this sample does not have a precoating of nickel unlike the other sample and the surface appears uniform.

The sample with 0.01 mm thick gold coating (figure 4.6) is not as smooth as the sample with the 0.5 thick gold coating (figure 4.5 (b)).

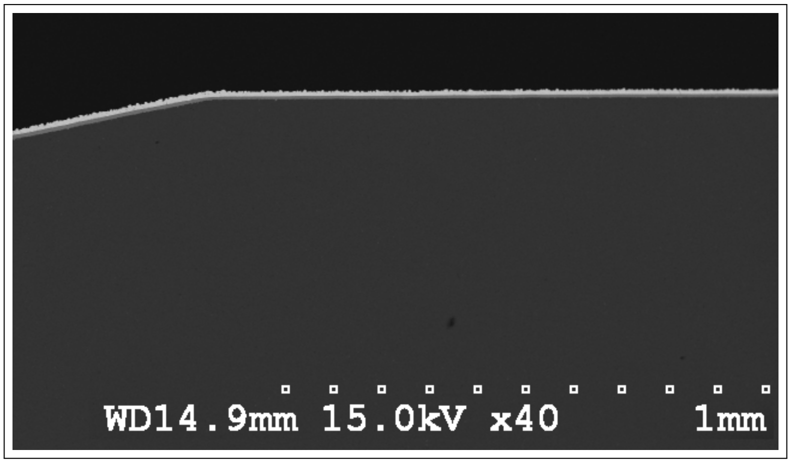

Figure 4.6: Surface of the 0.01 mm thick sample shown for the same scale as figure 4.5 (b).

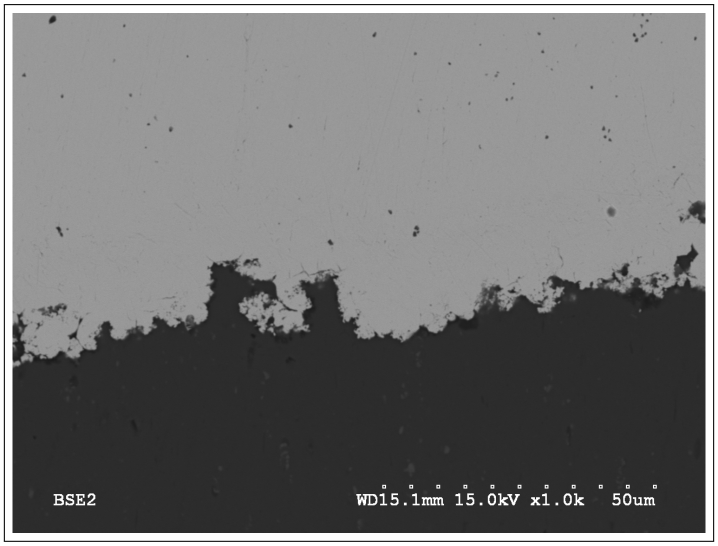

Figure 4.7: Detailed features of the gold-aluminum interface for the 0.5 mm thick sample shown for the same scale as figure 4.5 (a).

The bonding of the sample with the thicker coating of 0.5 mm is displayed on figure 4.7, where the gold is the area of light grey colour and the darker area is the aluminum. The gold appears to be well mixed with the aluminum, not only deposited superficially.

According to the figure 2.7 the thicknesses of the current samples are not optimum for photon production, but the purpose of the converter sample test is to characterize the interface properties of different cladding methods not to compare the photon production.

4.2.2 FIB examination

The FIB is capable of performing cross sections with its ion beam while showing the area that is being sectioned. Hence the sample does not have to be segmented with a cutting tool that can damage the interface.

In order to check if the FIB can perform cross sections of the samples a scrap piece of the sample with the 0.01 mm coating was tested in the Hitachi FB-2100 of the University of Victoria. This FIB uses a gallium beam with an accelerating voltage of 10 to 40 keV and a maximum current of 40 nA at 40 keV [1].

With the FIB, a rectangular surface of the coating was irradiated three times reducing the rectangle area irradiated each time to obtain a sufficient cross section. The FIB beam used had 40 kV, 0.62 nA and a dwell time of 3 μs. Figure 4.8 (a) shows the cross section of the sample enclosed in the yellow rectangle. The blue rectangle shows the depth that had been achieved at a previous irradiation using the same beam but with a dwell time of 25 μs. The largest area indicated by the red lines was the first area irradiated, using the same beam parameters. The operation was cancelled since the selected area was too large to generate a good result in a short period of time.

The deepest cross section wall (enclosed in the green rectangle fig. 4.8 (a)) was slightly polished with a beam of 40 kV and 0.73 nA.

To measure the coating thickness the sample was introduced into a SEM. Figure 4.8 (b) shows the thicknesses of the layers of gold and nickel. The thickness of the gold coating measured is 0.012 mm which confirms the result of the previous SEM examination. The nickel thickness measured on the cross section achieved with the FIB was 0.006 mm.

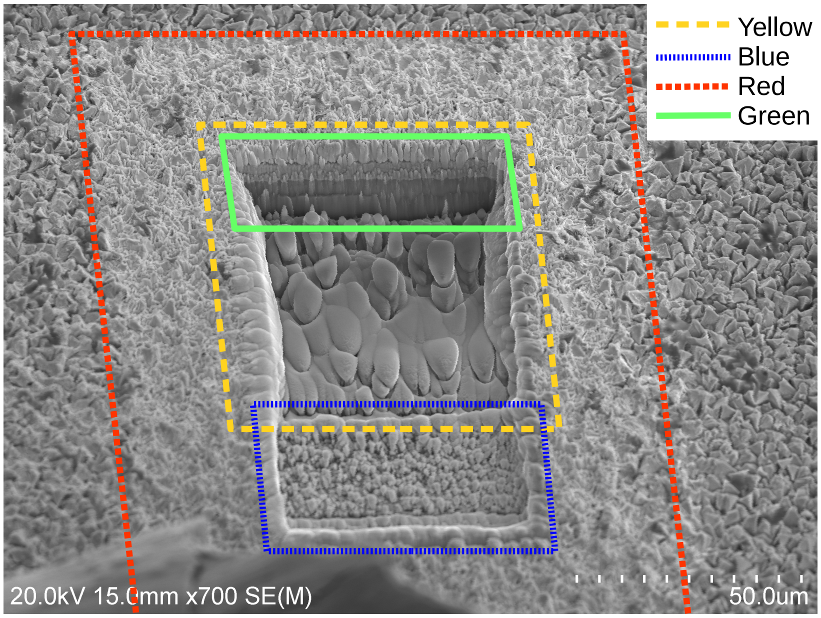

(a) Cross section

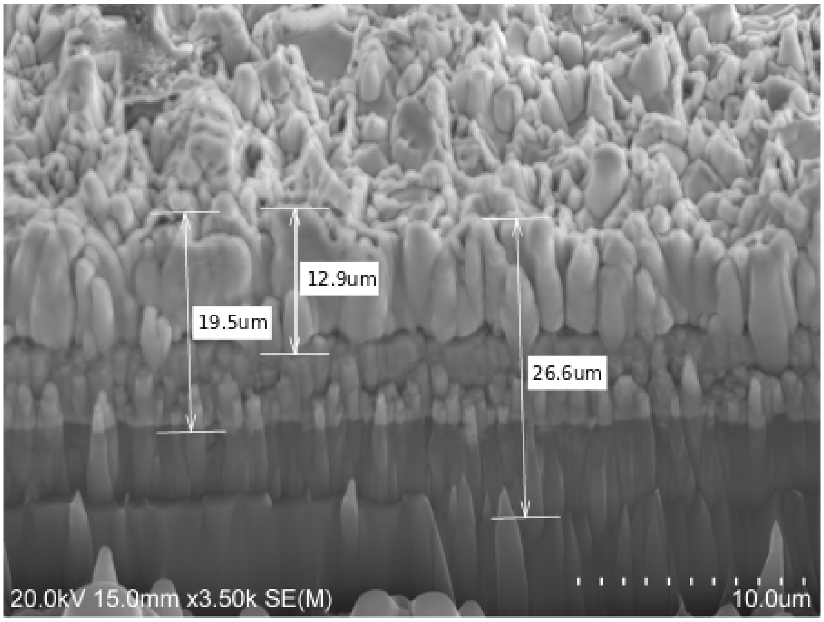

(b) Coating thickness

Figure 4.8: FIB cross section of the sample with a gold coating of 0.01mm. (a) shows the different depths achieved with the ion beam, and the pyramidal grain shape of the deposited gold. (b) displays the thickness of the gold coating of 12.9 μm, the nickel pre-coating layer of 6.6 μm and the penetration depth of the polishing beam of 26.6 μm.

With the FIB it was possible to visualize the grain of the sample. Figure 4.8 (a) shows the grained gold with a tetrahedral shape of the coating. This pyramidal shape could result in a lower thermal stress on the bonding, because the grain spacing could allow the expansion of the material when it is heated.

4.3 Converter sample test

The electron beam for the converter sample test stand is installed in the low energy section of the accelerator, having a beam energy of 300 keV with the beam power limited to 200 W for the first set of tests, later 3 kW will be available.

The sample tests will consist of measuring the temperature and current of samples when they are irradiated with the electron beam. After irradiation, a microscopic examination of the samples will look for the effects of the irradiation in the coating of the sample. In case that the coated samples do not present the desired quality and durability, the sample supplier company will not be used to manufacture the converter.

In the remainder of this section, operational considerations to perform these tests are described.

4.3.1 Converter sample irradiation

With COMSOL simulations, the temperature of the samples (aluminum cylinders with gold coating (fig. 4.3)) at the steady state was estimated (fig. 4.9). The model includes a sample in a holder clamp (fig. 4.2 b), cooled with two water pipes, using a Non-Isothermal Flow with a laminar approach.

To simulate the electron beam irradiation area, the heat source used in COMSOL was a gaussian profile of $\sigma = 0.335$ mm located on the centre of the coated face of the samples. Since the S_o of an electron beam of 300 keV in gold is 0.085 mm for the sample with gold coating of 0.5 mm thick the heat source was simulated on the surface of the coating. For the sample with a 0.01 mm thick gold coating, the heat source was simulated in the aluminum, taking into consideration the S_o of aluminum, 0.4 mm [19]. The S_o values referred to above were verified with Geant4 simulations.

For the simulations, the initial temperature assigned to the samples and the cooling water was $t_0 = 25$°C, and the flow rate was 0.04 l/s.The samples were simulated with the heat source set up to 5 W, 10 W, 20 W, 30 W, 40 W, 50 W, 100 W, 150 W and 200 W.

The maximum temperature of the sample with 0.5 mm gold coating was 367°C which is far from the melting point of the aluminum (fig. 4.10), therefore the sequences of power considered are safe to use to irradiate the samples.

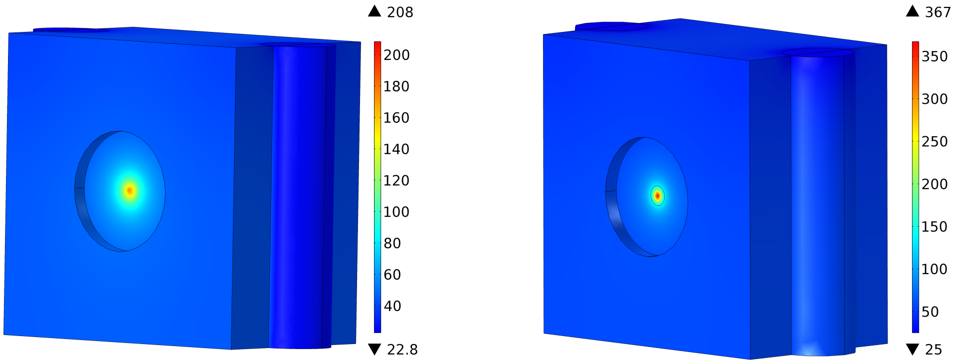

(a) 0.01mm Au coating

(b) 0.5mm Au coating

Figure 4.9: Temperature maps of the samples heated with the highest test power of 200 W. The color scale indicates °C.

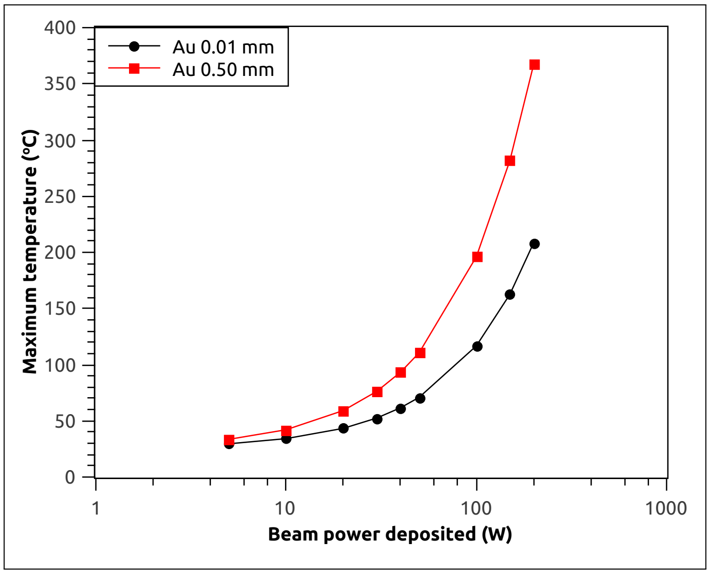

Figure 4.10: Maximum temperatures at the steady state of the samples heated with different powers.

The test procedure will start with the irradiation of the first out of 3 samples with a short pulse of 300 μs at 5 W, the temperature will be registered. Before using a higher power the sample should return to the initial temperature. After verifying that the maximum temperature reached by the first sample irradiated with all the range of powers is below the melting point of the aluminum, the irradiation time will be increased for the second sample in the holder and the procedure will be repeated. Finally, the last sample will be irradiated continuously during one hour.

The irradiation tests are expected to be performed by the end of 2016.

Chapter 5

Heat transfer coefficient

The heat deposited in the trench coating is transferred to the fin system by conduction, and the fins transfer the heat to the water cooling by means of forced convection. The convection heat transfer rate $\dot{q}$ is given by the Newton's law of cooling:

$$\dot{q}_{conv} = -hA[T(t) - T_f] \tag{5.1}$$

where A is the surface where the heat flows, $T(t)$ is the temperature of the body at the time t, and T_f is the temperature of the fluid away from the surface of the body. The heat transfer coefficient h depends on the properties of the fluid, the geometry of the surface, the nature of the movement of the fluid, and the volumetric velocity of the the fluid [6].

The particular heat transfer coefficient value of a fin system needs to be measured directly but can be estimated with [12].

$$h = \frac{Nu \cdot k}{L} \tag{5.2}$$

where Nu is the Nusselt number, k is the thermal conductivity of the water, and L is the length of the fins. The Nusselt number is given by equation 5.3

$$Nu = 0.0223 Re^{4/5} Pr^{0.4} \tag{5.3}$$

where Re and Pr are the Reynolds and the Prandtl number respectively. The Reynolds number depends on the flow velocity V, the length of the fins and the kinematic viscosity ν.

$$Re = \frac{V \cdot L}{\nu} \tag{5.4}$$

The Prandtl number is given by equation 5.5

$$Pr = \frac{c_p \mu}{k} \tag{5.5}$$

where c_p is the specific heat, μ is the dynamic viscosity and both are obtained from tables.

Q (ml/min)	**Estimated *h* (W/m^2 °C)**
100	206
240	377
500	667

Table 5.1: Theoretical heat transfer coefficient.

5.1 Heat transfer coefficient test

In order to find the heat transfer coefficient h for the fin system, a prototype of half of the converter model C without a gold coating was fabricated out of an aluminum 6061 block. The dimensions of the fin system prototype are shown in the figure 5.1. The prototype of the fins have covers on front, back and top in order to contain water for forced convective cooling (Figure 5.1 (c)). The cooling water enters through the cover marked with the number 2, and comes out from the exit on cover 4.

The top cover of the fin system prototype (figure 5.2) is made out of plexiglass in order to be able to see through it and detect promptly any boiling of the water. On top of the plexiglass lid are drilled orifices that give access to the corresponding fins under the lid. The drilled orifices have different depths to insert thermocouples in the fins.

To seal the side covers and the fin block of the prototype, rubber gaskets were used between the junctions. Between the plexiglass lid and the fins, RTV[1] silicone adhesive was used to seal the junction.

---

[1] Room temperature vulcanization

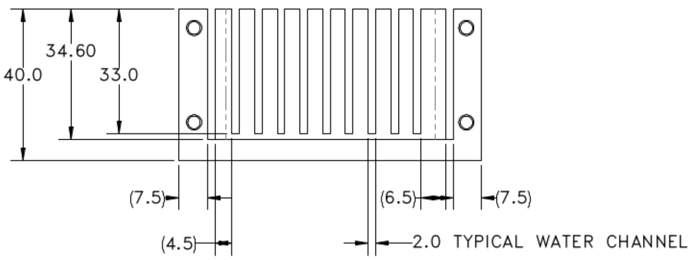

(a) Front view

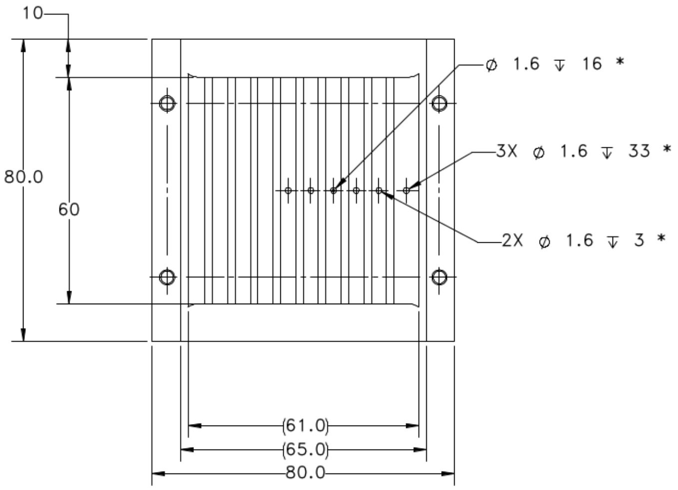

(b) Top view

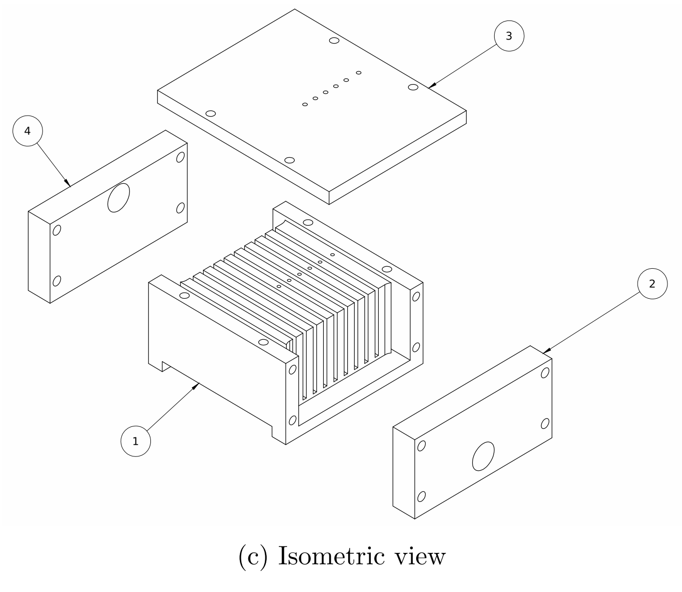

(c) Isometric view

Figure 5.1: Converter fin system prototype, (a) front view showing fin thicknesses and water channels, (b) top view showing the length of the fins, (c) isometric view showing lid (3), and covers with orifices for water entrance (2) and water exit (4).

Between the first fin and the wall of the fin system prototype, a layer of graphite was inserted to restrict the flow of water through that channel and to prevent heat dissipation, another identical graphite sheet was also inserted between the last fin and the wall (figure 5.2).

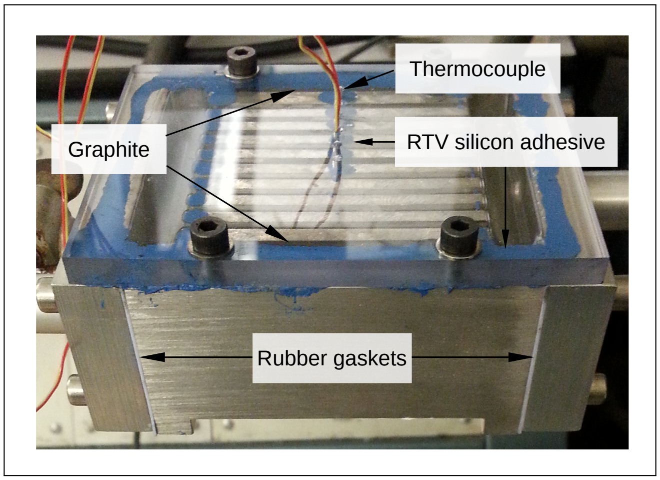

Figure 5.2: Details of the fin system prototype assembly.

The setup for the heat transfer coefficient test of the fin system prototype is shown in figure 5.3. The procedure for the test consisted of applying heat to the base of the fin system prototype until it reached a steady temperature, after which the heat source was removed.

The heat source used in this experiment was a ceramic heater with an area of 60 mm × 60 mm with a nominal power of 250 W at 220 V. The ceramic heater was connected to a three phase outlet that gave an average output voltage of 200 V.

The ceramic heater was attached to a graphite base and wrapped with a strip of polyester insulator to prevent the heat dissipation to undesired directions. A laboratory jack was used to make and remove contact between the ceramic heater and the fin system prototype.

An aluminum plate of 60×60×3 mm (figure 5.4) was fabricated to fit the ceramic heater ridges that were preventing an uniform contact between the ceramic heater and the fin system base. To improve the heat transfer contact between the ceramic heater and the aluminum plate, silicone heat sink paste was used, this paste was also used between the aluminum plate and the fin system prototype base. Silicone heat sink was also used on the end points of the thermocouples.

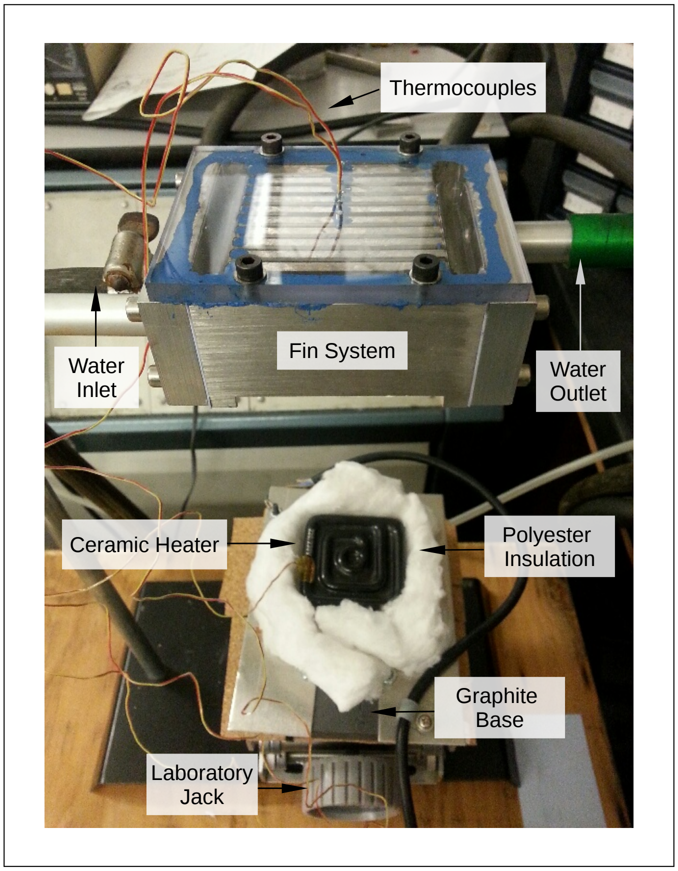

Figure 5.3: Experimental set up for obtaining the heat transfer coefficient.

Figure 5.4: Aluminum plate ridges that improve the contact between the ceramic heater and the fin system base.

The increment and the exponential decay of the temperature of the fins were registered with thermocouples connected to a data logger. There were four thermocouples available to continuously measure and register the temperature. Two of the thermocouples were used to measure temperature of two different fins, another thermocouple was used to register the temperature of the aluminum base and the last thermocouple measured the temperature of the water outlet tube.

The temperature of the inlet water was measured with a thermometer. The room temperature was monitored with a thermocouple independent of the data logger.

This experimental procedure was repeated for 3 different water flows, 100, 240 and 500 ml/min (table 5.2). The motivation to use different water flow rates was to estimate the minimum flow rate required to extract the maximum power of the heat source (205 W) and to see how using a larger water flow rate affects the temperature of the fin system.

Table 5.2 shows the estimated power that different flow rates of water are able to dissipate assuming a temperature difference of 30°C accoring to equation 3.1. Table 5.2 also shows the water velocity estimated for the fin system corresponding to each flow rate.

Flow rate (ml/min)	**Velocity (10^{-3}m/s)**	**Power (W)**
100	2.8	205
240	6.7	500
500	13.9	1000

Table 5.2: Flow rates and their respective water velocity for the converter used on the heat convective coefficient test and the corresponding power corresponding to ΔT=30°C.

Water was taken from a tap and its flow rate was regulated with a valve. Each flow rate was set up using a chronometer and a 500 ml graduated cylinder. The velocity of the water was then estimated using the flow rate and the diameter of the inlet pipe.

5.1.1 Heat transfer coefficient results.

Figure 5.5 compares the temperature profiles of a fin over the time for the flow rates considered in table 5.2. The fin starts at room temperature and then it increases until reaching steady state, after that the heat source is removed and the temperature decreases until it returns to room temperature. Figure 5.6 shows the maximum temperature registered for each flow rate. The largest difference between the initial and final temperature of the fin system was 37°C and corresponds to a flow rate of 100 ml/min.

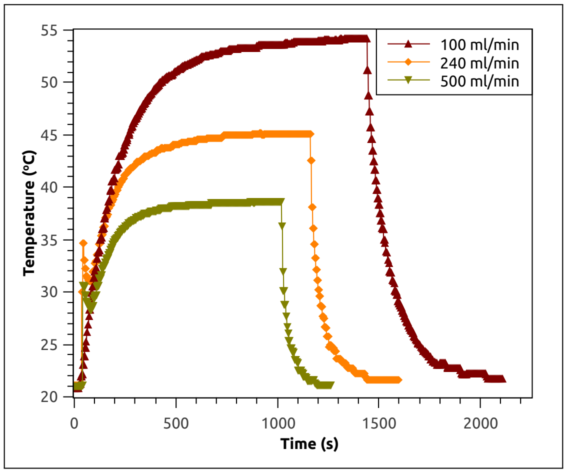

Figure 5.5: Temperature profiles of a fin for different flow rates.

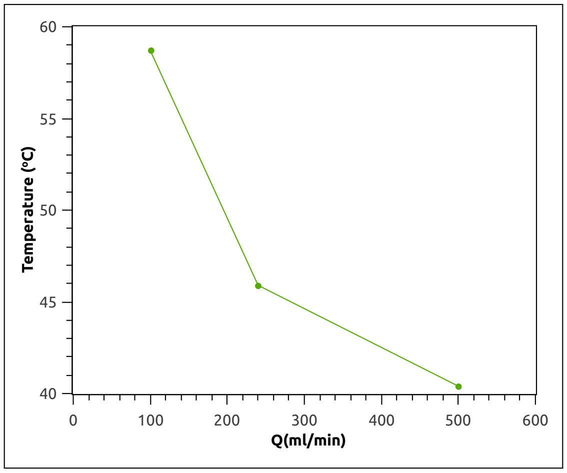

Figure 5.6: Maximum temperature of the fin system for different flow rates. The temperature decrease when increasing the flow rate.

An estimation of the heat transfer coefficient obtained using the equation 5.2 was compared with the heat transfer coefficient obtained using Newton's law 5.1. The area used for equation 5.1 was 0.04 m^2, $\dot{q}$ was 205.2 W, the difference of the maximum temperature and the initial temperature of the water measured is shown in the table 5.3. The heat transfer coefficient values obtained are compared in the table 5.4.

Q (ml/min)	**ΔT(C)**
100	26.9
240	12.4
500	6.8

Table 5.3: Water ΔT corresponding to the flow rates used.

	Heat transfer coefficient (W/m^2 °C)	
Q (ml/min)	**Experiment**	**Estimation**
100	188.2	206
240	408.3	377
500	744.6	667

Table 5.4: Comparision of the experimental and the theoretical heat transfer coefficient.

COMSOL was used to estimate the temperature rise of the fin system prototype using the initial conditions of the experiment. For the simulation the water velocity in the channels was not used, instead, the value of the experimental heat transfer coefficient was assigned to the wetted walls of the fins to account for the heat extraction. The maximum temperature of the fins obtained with the simulation is compared with the maximum temperature measured experimentally in figure 5.7. The biggest difference between the experiment and simulation occurs at the largest flow rate. The predicted heat transfer coefficient, table 5.4, is about 10% lower than the measurement, and the predicted temperature rise of the fin system is about 30% lower than the measurement. For the minimum flow rate, the difference between the temperature simulated and the experimental measurement is 0.5°C.

From Chapter 3 it was found that the minimum water velocity predicted to dissipate the power deposited in the converter was not enough to keep the water below 100°C, and larger velocities were needed. In this chapter it is found that for water velocities above the minimum required for certain power deposited, the heat transfer coefficient from estimations diverges from the experimental measurements (table 5.4). Therefore is essential to perform experiments to characterize the converter fin system for higher powers and higher velocities.

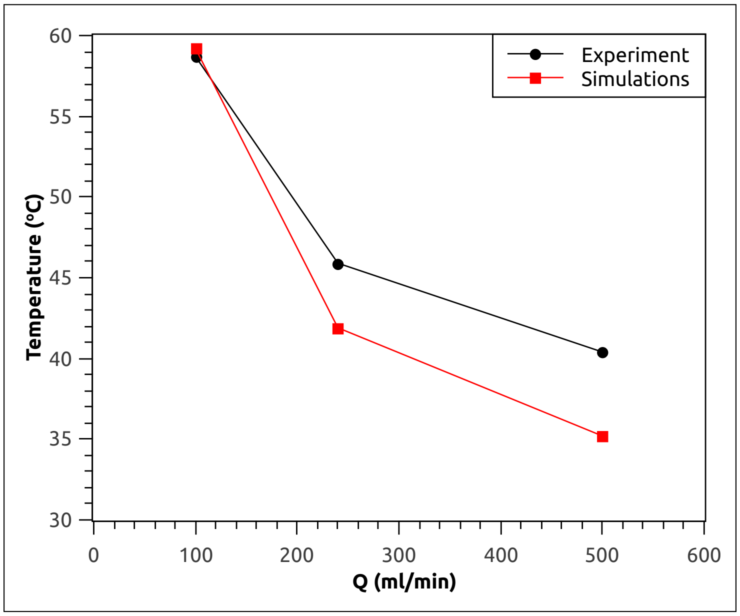

Figure 5.7: Maximum temperature of the fin system obtained experimentally and with COMSOL simulations for different flow rates.

Chapter 6

Conclusions

This thesis presents a number of studies necessary to optimize and verify the design of the ARIEL electron-to-gamma converter for the prodcution of rare isotopes.

The rate of isotope production through photofission was studied with Geant4 simulations which showed that for a fixed beam power, the maximum rate occurs for beam energies between 30 and 50 MeV.

Simulations were performed to verify the photon spectrum of the converter design for different materials and geometries. Gold, tantalum and tungsten were good candidates, but with the choice of aluminum as the heat sink material to reduce photon absorption, gold was chosen because its thermal expansion coefficient is close to that of aluminum.

According to simulations performed with Geant4 using an electron beam of 35 MeV to irradiate four converter models, a converter with a 2.0 mm thick aluminum base and a 0.2 mm thick gold coating has a satisfactory combination between photon production, and power absorption by the target and the converter itself. Also, the thickness of the aluminum base is favourable for machining. The power deposited in the converter was simulated in COMSOL and it was found that the amount of power deposited can be extracted by means of cooling water at a velocity of 4 m/s reaching a maximum temperature of 125°C on the converter spine, and a maximum temperature of the water of 92°C. Even though this is an achievable water velocity, the aluminum fin system will present erosion-corrosion due to the high velocity of the water cooling, so further studies have to be done on the fin system of the converter in order to optimize it.

A converter test stand was assembled in the electron hall to study the contact cladding techniques to be used in the converter. Preliminary electroplating samples were obtained from two different companies and they were examined under FIB and SEM to visually corroborate its union. An irradiation test is planned for the next run of the electron linac by the end of 2016.

Finally, experiments were performed to obtain the heat transfer coefficient of a fin system prototype. Even though the heat power applied was small compared to the one that will be absorbed in a operational mode, a methodology was established. Also, it was found that the heat transfer obtained experimentally using flow rates above the minimum required to dissipate the power applied differs from the heat transfer coefficient obtained with correlations. According to COMSOL simulations, the converter needs flow rates above the minimum estimated to dissipate the power absorbed and to keep the water cooling temperature under 100°C, therefore the heat transfer coefficient for the converter has to be obtained experimentally when using higher power and higher flow rates.

Appendix A

Geant4 Photofission

Geant4 10.2 was used to simulate the photon production and the photofission of the system.

The Livermore library, used to simulate the gamma production, is based on publicly evaluated data tables from the Lawrence Livermore National Laboratory (LLNL) [20]. The table used for the bremsstrahlung photons is the Evaluated Electrons Data Library (EEDL), which includes data to describe the transport of electrons, as well as the initial generation of secondary particles, such as the primary photon due to bremmstrahlung, as well as the primary electron due to inelastic scattering and electroionization [7]. The Livermore model has a validity range of 250 eV to 100GeV.

Even though Geant4 version 10.2 includes a photofission method it does not include production cross sections by default. The photo-fission cross section for ^{238}U used in our simulations was the empirical fit from reference [22] given by

$$\sigma(E_\gamma) = \sum_{i=1}^{2} \sigma_m(i) / \left[1 + \frac{(E_\gamma^2 - E_m^2)^2}{E_\gamma^2 \Gamma(i)^2} \right] \tag{A.1}$$

with the parameters values[24] shown in the table A.1, which gives the curve shown in figure A.1

Components	E_m **(MeV)**	σ_m **(mb)**	Γ **(MeV)**
1	10.727	60.311	2.004
2	14.432	170.244	4.952

Table A.1: Parameter for the fit correspondent to photofission

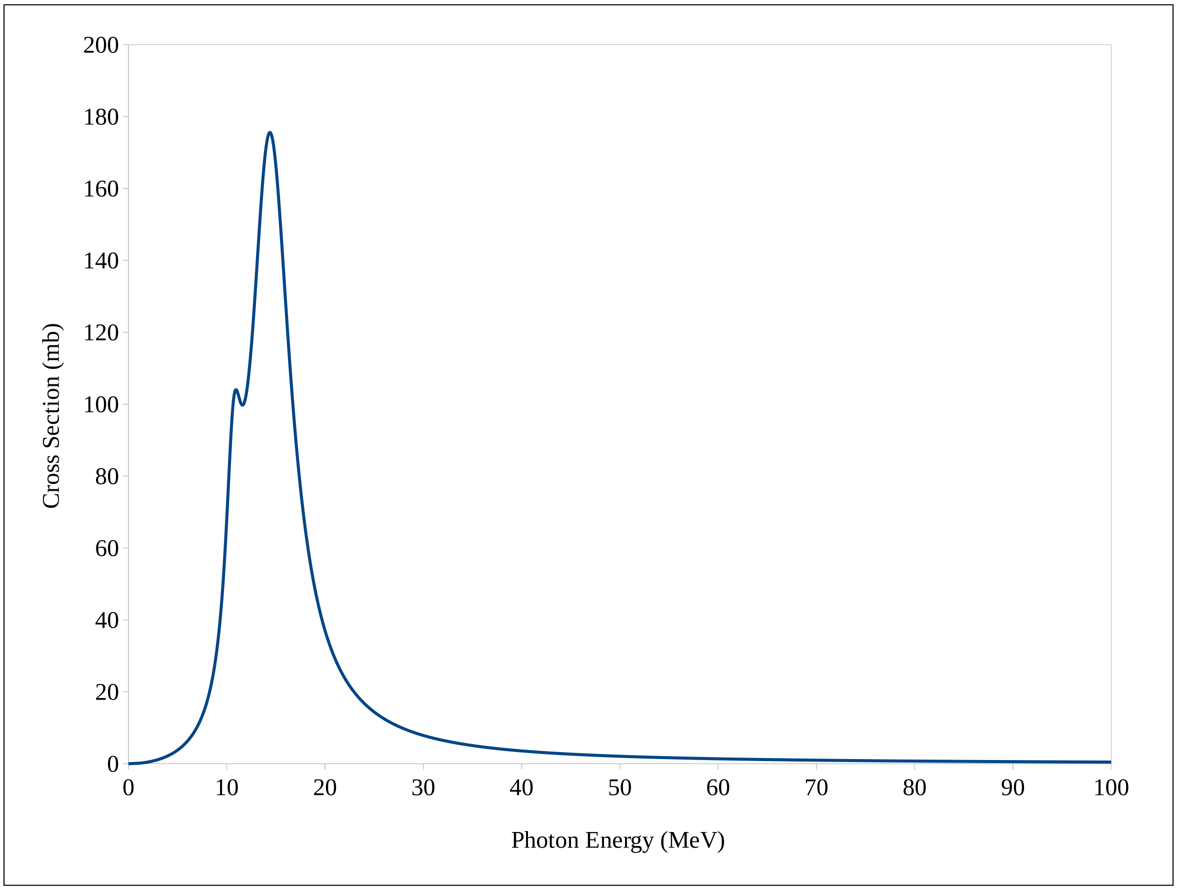

Figure A.1: Curve of the empirical fit of the photo-fission cross section for ^{238}U.

Bibliography

[1] Advanced microscopic facility at uvic. URL: `http://www.uvic.ca/research/advancedmicroscopy/about/microscopes/fib/index.php`.

[2] Comsol multiphysics. URL: `https://www.comsol.com`.

[3] S. Agostinelli, J. Allison, K. Amako, J. Apostolakis, H. Araujo, and P. Arce. Geant4a simulation toolkit. *Nuclear Instruments and Methods in Physics Research Section A: Accelerators, Spectrometers, Detectors and Associated Equipment*, 506(3):250 – 303, 2003.

[4] Nancy Bannach. Characterizing the flow and choosing the right interface. URL: `https://www.comsol.com/blogs/characterizing-flow-choosing-right-interface/`.

[5] Leroy C. Radiation interaction in matter and principles of detection. *AIP Conference Proceedings*, 2007.

[6] Çengel Y. and Boles M. *Termodinámica*. McGraw-Hill Companies, Inc, México, 2007.

[7] M. B. Chadwick, P. Obloinsk, and Herman. Endf/b-vii.0: Next generation evaluated nuclear data library for nuclear science and technology. *Nuclear Data Sheets*, 107(12):2931–3060, 2006.

[8] Merriman Colin. The fundamentals of explosion welding. *Welding Journal*, 85(7):27–29, 2006.

[9] Hobart Brothers Corp. *Guide for Aluminum Welding*, 2013.

[10] The engineering toolbox. Coefficients of linear thermal expansion. URL: `http://www.engineeringtoolbox.com/linear-expansion-coefficients-d_95.html`.

[11] The engineering toolbox. Thermal conductivity. URL: `http://www.engineeringtoolbox.com/thermal-conductivity-d_429.html`.

[12] Incropera F. and DeWitt D. *Fundamentals of heat and mass transfer*. McGraw-Hill Companies, Inc, United State of America, 3rd edition, 1990.

[13] Jackson John. *Classical Electrodynamics*. John Wiley & Sons, Inc., 1999.

[14] Werner Kern and Klaus K. Schuegraf. *Deposition Technologies and Applications: Introduction and Overview*. William Andrew Publishing, 2002.

[15] Lytron. Erosion-corrosion in cooling systems. URL: `http://www.lytron.com/Tools-and-Technical-Reference/Application-Notes/Erosion-Corrosion-in-Cooling-Systems`.

[16] Lebois M. and P. Bricault. Simulations for the future converter of the e-linac for the triumf ariel facility. *Journal of Physics: Conference Series*, 312(5), 2010.

[17] Weglowski M.St., Blacha S., and Phillips A. Electron beam welding -techniques and trends- review. *Vacuum*, 2016.

[18] Royal Society of Chemistry. Periodic table. URL: `http://www.rsc.org/periodic-table`.

[19] National Institute of Standards and Technology. Stopping power and range tables for electrons. URL: `http://physics.nist.gov/cgi-bin/Star/e_table.pl`.

[20] S. T. Perkins, D. E. Cullen, and S. M. Seltzer. Tables and graphs of electron-interaction cross sections from 10 eV to 100 GeV derived from the LLNL Evaluated Electron Data Library (EEDL), Z = 1 to 100. 31, November 1991.

[21] Koscielniak S. Ariel e-linac electron linear accelerator for photo-fission. *Springer*, 225, 2013.

[22] Cadwell J. T and Dowdy E. J. Giant resonance for the actinide nuclei: Photoneutron and photofission cross sections for ^{235}U, ^{236}U, ^{238}U, ^{232}Th. 21(4), 1980.

[23] S. Tavernier. *Experimental Techniques in Nuclear and Particle Physics*. Springer-Verlag Berlin Heidelberg, 2010.

[24] Cuong P. V. *Development of a new surface ion-source and ion guide in the ALTO project.* Theses, Université Paris Sud - Paris XI, December 2010.

[25] G.H. Zschornack. *Handbook of X-Ray Data.* Springer Berlin Heidelberg, 2007.